

Lund University GEM thesis series nr 23

# Study of radiometric variations in Unmanned Aerial Vehicle remote sensing imagery for vegetation mapping

**Ximena Tagle**

---

2017

Department of Physical Geography and Ecosystem Science

Lund University

Sölvegatan 12

S-223 62 Lund



**LUND**  
UNIVERSITY



**UNIVERSITY OF TWENTE.**

**ITC**

FACULTY OF GEO-INFORMATION SCIENCE AND EARTH OBSERVATION



# Study of radiometric variations in Unmanned Aerial Vehicle remote sensing imagery for vegetation mapping

by

Ximena Tagle

---

Thesis submitted to the department of Physical Geography and Ecosystem Science,  
Lund University, in partial fulfilment of the requirements for the degree of Master of  
Science in Geo-information Science and Earth Observation for Environmental  
Modelling and Management

Thesis assessment Board

First Supervisor: *Dr., Lars Eklundh* (Lund University)

Exam committee:

Jonas Ardö, Lund University

Hongxiao Jin, Lund University

## Disclaimer

This document describes work undertaken as part of a program of study at the University of Lund. All views and opinions expressed therein remain the sole responsibility of the author, and do not necessarily represent those of the institute.

Course title: Geo-information Science and Earth Observation for Environmental Modelling and Management (GEM)

Level: Master of Science (MSc)

Course duration: January 2017 until June 2017

Consortium partners:

The GEM master program is a cooperation of departments at 5 different universities:

University of Twente, ITC (The Netherlands)

University of Lund (Sweden)

University of Southampton (UK)

University of Warsaw (Poland)

University of Iceland (Iceland)

# Abstract

Unmanned Aerial Vehicles (UAVs) provide a flexible method for acquiring high-resolution imagery with relative simple operation and cost-effectiveness. This technology emerged 30 years ago and it is widely used by commercial, scientific, and military communities due to its versatility. However, new technology brings new challenges. One of them is the radiometric accuracy of the UAV imagery. Radiometric accuracy is especially important when working with different illumination conditions, dates or sensors.

The present study focuses on reducing radiometric errors of UAV images for vegetation mapping. The fieldwork took place from September 2016 to May 2017 in an agricultural area and a mire. The effect in incident light variations was studied flying at different dates and at different times of the day. Sun elevation angle and presence of clouds gave significant variations in UAV imagery. The study of the sun elevation angle showed that suitable hours for UAV surveys at higher latitudes surveys is within 2 hours of solar noon, since the amount of shadows is low because the sun elevation angle is between 20° and 40° during autumn, spring and summer.

The difference in the type of radiation affected the homogeneity of the UAV imagery and the radiometric correction, making the correction of UAV imagery from days with clear sky more difficult, when the direct radiation is predominant. The BRDF effects were less pronounced under overcast conditions, when the predominant incident radiation is diffuse.

Nine correction methods were tested, and their effect on different vegetation indices was compared, showing that the irradiance correction method prior to an empirical line calibration provide less errors than other methods. However, the errors are still high when compared with ground spectral samples (lowest RMSE 38% under overcast conditions for the NDVI).

A simple workflow was developed for vegetation mapping purposes for the Micasense Rededge camera. We suggest to use the automatic dark current-corrected and automatic reduced vignetting effect images, plus irradiance compensation and the use of empirical line calibration to obtain reflectance values in single images before generating the orthomosaic. The radiometric correction process should be done for each spectral band, having a new calibration equation per mission due to the change in sky conditions.

Unfortunately, this workflow will not provide accurate results in the calculation of vegetation indices that assess small variations like the case of chlorophyll indices or vegetation indices that combine several bands. Further research is needed to improve the accuracy of the correction.

**Keywords:** UAV, radiometric correction, vegetation mapping, vegetation indices

To my family and all the amazing people I met during this journey.

*En especial para tí pa!*

# Acknowledgments

I would like to thank my supervisor Lars Eklundh, who supported and guided me during the whole thesis period. I am very thankful with Per-Ola Olsson and Hongxiao Jin from the RS group for helping me with technical details every time I needed. Thank you Per-Ola for your patience!

I also would like to thank Leif Klemedtsson and Bengt Liljeblad from University of Gothenburg, for providing all the facilities to work at Skogaryd.

This research was supported by the Education, Audiovisual and Culture Executive Agency (EACEA) who provided the Erasmus+ scholarship; the Department of Physical Geography and Ecosystem Science (INES) who provided the equipment; and the Department of Biosystems and Technology at SLU who provided access to the Lönnstorp research station.

I would like to give special thanks to Joy, Moncho and Mirza, who had to deal with me during this time. Thank you so much!!

# Contents

Abstract.....	i
List of Tables .....	v
List of Figures .....	vi
List of Abbreviations .....	viii
1. Introduction .....	1
1.1. Background .....	1
1.2. Aims.....	3
2. Remote Sensing with UAVs.....	4
2.1. Unmanned Aerial Vehicles (UAV) .....	4
2.2. Geometric Correction .....	6
2.3. Radiometric Correction.....	8
2.4. Vegetation indices.....	11
3. Methodology.....	13
3.1. Study area .....	13
3.2. UAV characteristics.....	14
3.2.1. Explorian 8 UAV .....	14
3.2.2. Payload.....	14
3.3. Software characteristics.....	16
3.4. Method .....	18
3.4.1. Data collection .....	20
3.4.2. Data processing.....	24
4. Results.....	35
4.1. Incident light variation in UAV imagery .....	35
4.2. Radiometric variations in vegetation indices.....	42
4.2.1. Chlorophyll index .....	46
4.2.2. Green ratio index .....	46
4.2.3. Structural indices .....	47
4.3. Suggested radiometric correction workflow .....	50
5. Discussion.....	52
5.1. Incident light variation in UAV imagery .....	52

5.2.	Radiometric variations in vegetation indices.....	53
5.3.	Limitations and advantages .....	54
5.4.	Recommendations .....	56
6.	Conclusions .....	57
7.	References .....	59

## List of Tables

<b>Table 1</b>	Performance comparison of UAVs and other platforms.....	5
<b>Table 2</b>	Primary vegetation indices used in UAV-based remote sensing .....	12
<b>Table 3</b>	Explorian 8 specifications.....	14
<b>Table 4</b>	Specifications of the sensor used.....	15
<b>Table 5</b>	Spectral information of the MicaSense RedEdge camera .....	15
<b>Table 6</b>	Information of the UAV missions performed. “S” corresponds to Skogaryd and “L” to Lönnstorp .....	22
<b>Table 7</b>	Radiometric correction methods compared.....	25
<b>Table 8</b>	Reflectance averages per band per reflective target.....	29
<b>Table 9</b>	Results of the Shapiro-Wilk’s test to determine if the replicates of the spectral measurements have a normal distribution per target. ....	29
<b>Table 10</b>	Data collected and orthomosaics generated per mission. The highlighted missions were used for the radiometric correction comparison. ....	33
<b>Table 11</b>	Vegetation indices used for the radiometric correction comparison.....	34
<b>Table 12</b>	Results of the Kruskal-Wallis rank sum test to determine the Lambertian properties of the reflective targets.....	37

# List of Figures

<b>Figure 1. a)</b> Picture of a fixed-wing Usense-X8 UAV. <b>b)</b> Picture of rotorcraft Explorian 8 UAV. ....	4
<b>Figure 2</b> Simplified radiance diagram for an optical sensor -mounted in a low flying altitude platform....	8
<b>Figure 3</b> Study area a) Mycklemossen mire, b) Lönnstorp agricultural area .....	13
<b>Figure 4</b> Spectral response curve for the Micasense RedEdge camera. The colors of the lines correspond to the camera bands. The brown line is a standard reflectance profile of a green vegetation canopy. ....	16
<b>Figure 5</b> RGB orthomosaic and DSM generated on a) Pix4D mapper, b) Atlas and c) Agisoft PhotoScan Pro for the same mission in Lönnstorp. ....	17
<b>Figure 6</b> Workflow for processing multispectral UAV imagery to generate a vegetation index map from one UAV mission. ....	19
<b>Figure 7</b> Mission planned in UgCS for the agricultural field on Lönnstorp .....	20
<b>Figure 8</b> Pictures of the sky condition classes in Lönnstorp before the flights: a) Overcast, b) Partly cloudy and c) Clear sky. ....	21
<b>Figure 9</b> Targets distribution scheme during a UAV mission. The distribution could vary according to the extent of the mission and the characteristics of the study area. ....	23
<b>Figure 10</b> View angles of the spectrometer during the ground reflectance measurements. ....	23
<b>Figure 11</b> Map of the validation samples location during the clear sky mission (Lönnstorp_24-03-17). ..	24
<b>Figure 12</b> Spectral signature of 5 reflective targets used for the empirical line calibration. Grey lines are the replicates and the black line is the average. ....	28
<b>Figure 13</b> Linear regression of the ELC with all the reflective targets. MM stands for Mosaic Mill and MS for Micasense reflective targets. ....	31
<b>Figure 14</b> Linear regression of the ELC with four reflective targets. MM stands for Mosaic Mill and MS for Micasense reflective targets. ....	32
<b>Figure 15</b> Irradiance measured at the ground by the field spectrometer with cosine corrector of 180° during different dates and sky conditions. ....	35
<b>Figure 16</b> Reflectance of the calibration targets per illumination conditions. ....	36
<b>Figure 17</b> RGB orthomosaics generated in Agisoft Photoscan without any radiometric correction from Skogaryd missions. They are organized from the lowest sun elevation angle to the highest. ....	38
<b>Figure 18</b> RGB orthomosaics generated in Agisoft Photoscan without any radiometric correction from Lönnstorp missions. They are organized from the lowest sun elevation angle to the highest. ....	39
<b>Figure 19</b> Overlay of the histograms from the orthomosaics with different sun elevation angles for the red and NIR bands. a) Clear sky in Lönnstorp, b) Partly cloudy sky in Skogaryd, c) Overcast conditions in Lönnstorp. ....	40
<b>Figure 20</b> Boxplot of pixel values of beetroot (Beet), MM target of 10% reflectance (MM10), soil and winter rye (Grass) corresponding to the NIR and Red edge bands of the orthomosaics under 29° and 44° of sun elevation. ....	42
<b>Figure 21</b> RGB orthomosaics generated in Agisoft Photoscan with different radiometric correction methods under clear sky conditions (Lönnstorp 24-03-2017)/ .....	43
<b>Figure 22</b> RGB orthomosaics generated in Agisoft Photoscan with different radiometric correction methods for a mission under overcast conditions (Lönnstorp 08-04-2017) .....	44

<b>Figure 23</b> Histograms of the orthomosaics generated with different radiometric correction methods of the overcast mission (Lönnpstorp 08-04-2017). The colors of the lines correspond to the camera bands. .	45
<b>Figure 24</b> RMSE statistics (%) for radiometric correction method comparison on TCARI/OSAVI of the clear sky mission. ....	46
<b>Figure 25</b> RMSE statistics (%) for radiometric correction method comparison in the G/R index .....	47
<b>Figure 26</b> RMSE statistics (%) for radiometric correction method comparison on the NDVI.....	48
<b>Figure 27</b> NDVI of the orthomosaics generated with different radiometric correction methods for a mission under overcast conditions (Lönnpstorp 08-04-2017). ....	49
<b>Figure 28</b> RMSE statistics (%) for radiometric correction method comparison on the NDRe index .....	49
<b>Figure 29</b> RMSE statistics (%) for radiometric correction method comparison on the EVI.....	50
<b>Figure 30</b> Suggested radiometric correction workflow. ....	51

# List of Abbreviations

UAV	Unmanned Aerial Vehicle
RS	Remote Sensing
SFM	Structure from Motion
FOV	Field of View
DN	Digital Number
EM	Electromagnetic
GPS	Global Positioning System
RTK	Real Time Kinematic
GCP	Ground Control Point
DSM	Digital Surface Model
SITES	Swedish Infrastructure for Ecosystem Science
TOW	Take-off weight
GLONASS	Globalnaya Navigazionnaya Sputnikovaya Sistema
DLS	Downwelling Light Sensor
RGB	Red Green Blue
Re	Red edge
NIR	Near Infrared
TIR	Thermal Infrared
PFT	Plant Functional Type
BRDF	Bidirectional Distribution Function
EC	Eddie Covariance
NOAA	National Oceanic and Atmospheric Administration
RMSE	Root Mean Square Error

# 1. Introduction

## 1.1. Background

Unmanned Aerial Vehicles (UAV) provide a flexible method for acquiring high-resolution imagery with relative simple operation and cost-effectiveness (Feng et al. 2015). This technology emerged 30 years ago and it is widely used by commercial, scientific, and military communities due to its versatility (Liu et al. 2016). However, implementing new technology brings new challenges. Some of them are related to the radiometry of the images. Radiometry is the relationship between pixel values and the target radiance (Lebourgeois et al. 2008). The present study is focused on reducing radiometric errors of UAV images for vegetation mapping.

Vegetation mapping is the action of representing plant cover in a specific area. This task is highly necessary for interpretation and description of the environment because vegetation is related to soils, climate and other ecological factors (Pedrotti 2012). It provides valuable information to land use planners and ecologists to develop strategies regarding ecosystem services, climate change adaptation, among others (Nex and Remondino 2013; Zweig et al. 2015).

In order to generate vegetation maps, remote sensing (RS) is widely used. RS is a technique for gathering information by using a device separated from the target. In this case, the main target are plants and the devices could be sensors located on platforms such as satellites, airplanes or Unmanned Aerial Vehicles (Jones and Vaughan 2010).

Traditional RS technologies such as satellites and airborne are still useful for vegetation mapping but they have some technological, operational and economic constraints. Satellites can map large areas at the same time, however the spatial resolution of the acquired data is coarse. Sometimes they have higher spatial resolution, but the acquisition cost is higher as well. In addition, they may suffer from cloud cover and from constraints in relating imagery timing to specific phenologic phases because of the fixed-timing acquisitions. On the other hand, airborne surveys can be planned more flexibly, but organizing a campaign can be difficult and costly (Nex and Remondino 2013; Lillesand and Kiefer 2014; Feng et al. 2015; Matese et al. 2015).

UAVs have certain advantages over satellite-based or airborne platforms by providing cloud-free imagery with very high spatial resolution, relative simple operation, cost-effectiveness, reliability, greater autonomy, flexibility and safeness (Dunford et al. 2009; Laliberte 2009; Feng et al. 2015; Liu et al. 2016). However, they can only cover relative smaller areas due to lower platform endurance compared with airborne. Another drawback of the UAV platforms is the strong dependency on the weather conditions, such as wind or rain, on the flight ability. Nevertheless, UAVs allow to plan missions on the same location, resulting in longitudinal data which allow dynamical studies of temporal effects. For this reason UAVs have a high potential in vegetation studies (Dunford et al. 2009; Salamí et al. 2014).

In vegetation mapping, UAVs with multispectral cameras allow the calculation of different vegetation indices, making possible to perform several analysis such as plant cover quantification, identification of plant species composition and structure, among others (Laliberte 2009; Arnold et al. 2013; Nex and Remondino 2013). These techniques are crucial to fulfill the gap between in situ measurement and space borne observation, and it may contribute not only to the validation of the satellite-based models, but also to up-scaling the site-specific models (Sharma et al. 2012).

In order to generate accurate products for vegetation mapping, it is necessary to tackle the major constraints of UAV imagery: geometry and radiometry. Since UAVs are relative small, they tend to have less sensor stability during the flights, geometric accuracy tends to be lower compared to the data coming from piloted aircrafts. Yet, this issue is compensated by the vast amount of overlapping images taken by the UAV sensor and using Structure from Motion algorithms (SFM) (Fuyi et al. 2012; Huang et al. 2013). Unfortunately, radiometry has not been studied as thoroughly as image geometry. The variety of digital cameras being used with different (and sometimes unknown) characteristics, makes difficult to determine the quality of the data obtained (Kuusk and Paas 2007; Clemens 2012; Liu et al. 2016).

There are different factors that can contribute to radiometric errors during the flights. Some of them are: (1) the use of wide field of view (FOV) imaging equipment that creates an inherent radial variation in viewing angle, (2) the solar motion that creates a non-static illumination source, and (3) even though multispectral UAV imagery is cloud-free, clouds influence the incoming solar radiation at the surveyed area generating darker spots. This leads to variation on the Digital Number (DN) values for the same object and therefore, the stitching of the overlapping images cannot be done correctly (Dunford et al.

2009; Honkavaara 2014; Liu et al. 2016; Stark et al. 2016). For this reason, radiometric correction methods are necessary to overcome these challenges.

Radiometric correction in RS involves: (1) Correction of the vignetting effect (the fall of brightness on an image frame), dependent on the optics of the sensor; (2) reflectance correction, dependent on the sun azimuth, surface reflection, topography and illumination; and (3) atmospheric correction, dependent on atmospheric scattering (Honkavaara 2014; Lillesand and Kiefer 2014).

When comparing UAV technology with traditional RS, the latter already has an established radiometric correction process, while in UAV technology, this is still being researched (Clemens 2012; Aasen et al. 2015; Wang and Myint 2015). In consequence, it is necessary to study methods that could allow an improvement of radiometric accuracy of UAV remote sensing products for vegetation mapping.

## **1.2. Aims**

The main aim of this research is to study radiometric variations in UAV remote sensing products obtained with a multi-rotor UAV with a multispectral camera up to a level sufficient for vegetation mapping. The specific objectives are to:

- Analyze incident light variations in UAV imagery.
- Determine if radiometric variations propagate to vegetation indices.
- Suggest a workflow based on the knowledge obtained during the study.
- Identify limitations and advantages of UAV imagery for vegetation mapping focusing on radiometric constraints.

## 2. Remote Sensing with UAVs

### 2.1. Unmanned Aerial Vehicles (UAV)

The term UAV is applied to any aerial platform that is capable to fly without a person on board, independent of its level of autonomy. UAVs are also known as Unmanned Aerial System (UAS), Remotely Piloted Vehicle (RPV), Remotely Operated Aircraft (ROA), Remotely Piloted Aircraft (RPA), Unmanned surface vehicle (USV), and drone, among others (Salamí et al. 2014; Hajiyev et al. 2015; Liu et al. 2016).

UAVs platforms are diverse. They have similar design features of a full-scale aircraft. For this reason, they can be (1) fixed-wing, when they use the forward airspeed to generate lift, like airplanes; or (2) rotorcraft, when the wings revolve around a fixed mast called rotor to generate lift, like helicopters (one rotor blade) or quadcopters (four rotors), see Figure 1. In both cases, the main characteristics are: they are compact, they have a relative low cost, low speed, low ceiling altitude, light weight, low payload and short endurance. Also, they need a ground station to communicate with the airframe (Huang et al. 2013; Salamí et al. 2014; Liu et al. 2016).

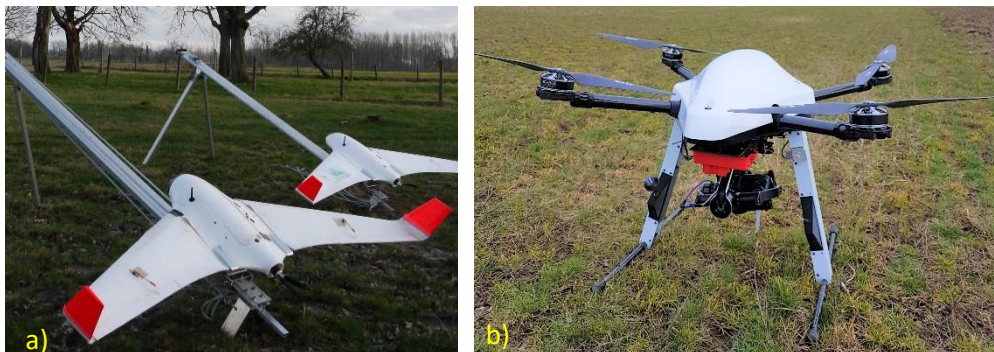


**Figure 1. a)** Picture of a fixed-wing Usense-X8 UAV. **b)** Picture of rotorcraft Explorian 8 UAV.  
Source a): <http://www.usense.be>

As previously mentioned, UAVs have many advantages compared with traditional remote sensing platforms. UAVs provide high spatial resolution imagery (usually less than 25 cm) collected at a relative low cost, and they have high temporal resolution due to the high flexibility of the UAV operation (Table 1). However, it is important to mention that UAV technology is more likely to complement traditional

RS instead of replacing it. UAV products contribute with validation of RS models and it will help filling spatial gaps (Dunford et al. 2009; Sharma et al. 2012; Liu et al. 2016).

**Table 1** Performance comparison of UAVs and other platforms.

✓✓✓ High   ✓✓ Medium   ✓ Low performance

Attributes	Satellites	Manned Aircrafts	UAVs
Endurance	✓✓✓	✓✓	✓
Payload capacity	✓✓	✓✓✓	✓
Cost	✓✓	✓	✓✓
Images without cloud coverage	✓	✓✓	✓✓✓
Maneuverability	✓	✓✓	✓✓✓
Deployability	✓	✓✓	✓✓✓
Autonomy requirement	✓✓	✓	✓✓

**Source:** Modified from *Liu et al. (2016)*

There have been several studies that demonstrated the potential of UAVs in the field of vegetation mapping. Salamí et al. (2014) note that most of the vegetation studies have focused on crop fields where the scan area is limited and well known. Nevertheless, the authors mention that there is also a significant number of studies on wildlands, including rangelands and forest.

Salamí et al. (2014) described three types of applications of UAVs for vegetation mapping, namely (1) passive, (2) proactive and (3) reactive. Passive applications use UAVs to collect information, but they do not perform any direct action on the vegetation in the short term. Some examples are estimating canopy cover and monitoring vegetation change. Proactive applications typically use UAVs to monitor the vegetation status, and more specifically to detect areas of disease, nutrient deficiency, invasive weeds, pathogens and drought. They differ from passive application in that the collected data is used to make decisions on short-term actions. In the case of reactive applications, UAVs are used to generate immediate responses at the same moment that a situation is detected. Although currently is not yet very common, in the near future UAVs would increase their autonomous ability to make decisions and perform actions.

Current studies strive for developing fully-autonomous UAVs in order to minimize the need for human control and the effects of human error. For instance, some UAVs have incorporated Real Time Kinematic

devices (RTKs) on their platforms to obtain more accurate locations, but most of UAVs need Ground control points (GCPs) to improve geometric accuracy.

However, this technology brings new challenges, especially when there is a lack of standardization at all levels, from sensors, vegetation indices, operational methods, UAV sizes and models, and automation of pilot capabilities (Hajiyev et al. 2015; Liu et al. 2016). Some of the present-day challenges are the limited accuracy of position and orientation data, synchronization issues between imaging sensors and ground control points, high roll and pitch variation between images, perspective distortion, and high variability in illumination conditions (Liu et al. 2016).

These challenges are mainly related to the stability and characteristics of the sensors, which in most of the cases is a light weight and small digital camera with limited power requirements and with a potential to store hundreds of images. Yet, as mentioned before, there is a lack of standardization of capabilities. Hence, there is a high diversity of digital cameras being used with different (and sometimes unknown) characteristics that makes difficult to determine the quality of the data obtained with the UAV (Kuusk and Paas 2007; Clemens 2012; Liu et al. 2016).

When it comes to processing of UAV data, one of important goals would be to obtain an automated image processing workflow. Automatization and standardization of processing UAV image data still is not on a level of RS data. As mentioned previously, major constrains in the processing workflow are geometry and radiometry of UAV imagery, and the lack of automatization and standardization of the calibration processes.

## 2.2. Geometric Correction

Photogrammetry is the science and technology of obtaining spatial measurements and other geometrically reliable derived products from photographs (Lillesand and Kiefer 2014). In order to reduce the difference between objects location in the images and their location in the real world, geometric calibration it is performed. A common way to improve geometric accuracy is by geo-referencing the RS product with Ground Control Points (GCPs). The distribution and number of GCPs change the geometric accuracy of the product (Wijesingha 2016).

Nevertheless, issues of geometric accuracy in UAV imagery are reduced using novel computer vision techniques such as Structure-From-Motion (SFM) and Multi-View Stereo (MVS). Structure-from-Motion represents an effective, low-cost topographic surveying tool. It needs a vast amount of overlapping images taken by consumer-grade digital cameras or more sophisticated sensors to generate an orthomosaic or DSM (Fuyi et al. 2012; Westoby et al. 2012).

Currently, there are several software capable of perform SFM. Some of the open source tools are APERO, MICMAC, VisualSFM and OpenMVG. Some of the commercial options are Agisoft Photoscan, Pix4D and Atlas (Dall 'asta and Dicatea 2014). The following workflow belongs to Agisoft Photoscan Professional, but most of the software follow a similar outline, having algorithm variations.

**(1) Feature extraction across the photos (Alignment).**

PhotoScan detects points in the source photos which are stable under viewpoint and lighting variations and generates a descriptor for each point based on its local neighborhood. The descriptors are used to detect correspondences across the photos and align them. This is similar to the SIFT (Scale-invariant feature transform) approach used in other software, but it uses different algorithms for a little bit higher alignment quality (Semyonov 2011; Agisoft LLC 2016).

**(2) Solving for camera intrinsic and extrinsic orientation parameters (Sparse point cloud creation).**

PhotoScan uses a complex algorithm to find approximate camera locations and refines them later using a bundle-adjustment algorithm that generates a sparse point cloud. The sparse point cloud is a set of matching image data points in a three-dimensional coordinate system (Semyonov 2011; Agisoft LLC 2016).

**(3) Dense surface reconstruction (Dense point cloud generation).**

Several processing algorithms are available. Exact, Smooth and Height-field methods are based on pair-wise depth map computation, while Fast method utilizes a multi-view approach to generate a 3D dense point cloud (Semyonov 2011; Agisoft LLC 2016).

### 2.3. Radiometric Correction

Radiometry is the science of measuring light in any portion of the electromagnetic (EM) spectrum. It is important to consider radiometry when working with optical sensors since the recorded images depend on the sunlight.

Figure 2 shows a simplified diagram of how an optical sensor mounted in a low flying altitude platform records information. As shown in the figure, the incident radiation comes from the sun, which is the EM radiation source. This radiation is partly absorbed by the atmosphere, some is scattered in the atmosphere, part is absorbed by different surface elements and one fraction is reflected by the surface elements (Honkavaara 2014; Humboldt State 2015).

The aim of optical sensors is to register radiation reflected from the surface. However, the recorded data (DN values) do not coincide with the reflectance of the same object measured from a short distance (ground observations). This is due to the characteristics of the sensor such as color processing algorithms, camera settings, vignetting and flying altitude. It is also due to the variation of environmental factors like sun's azimuth and elevation, atmospheric conditions such as fog or aerosols and the reflectivity of the surrounding objects. For this reason, conversion of DN values to surface reflectance is needed. This process is known as radiometric calibration and it is performed before other image processes (Lebourgeois et al. 2008; Mitchell 2010; Humboldt State 2015).

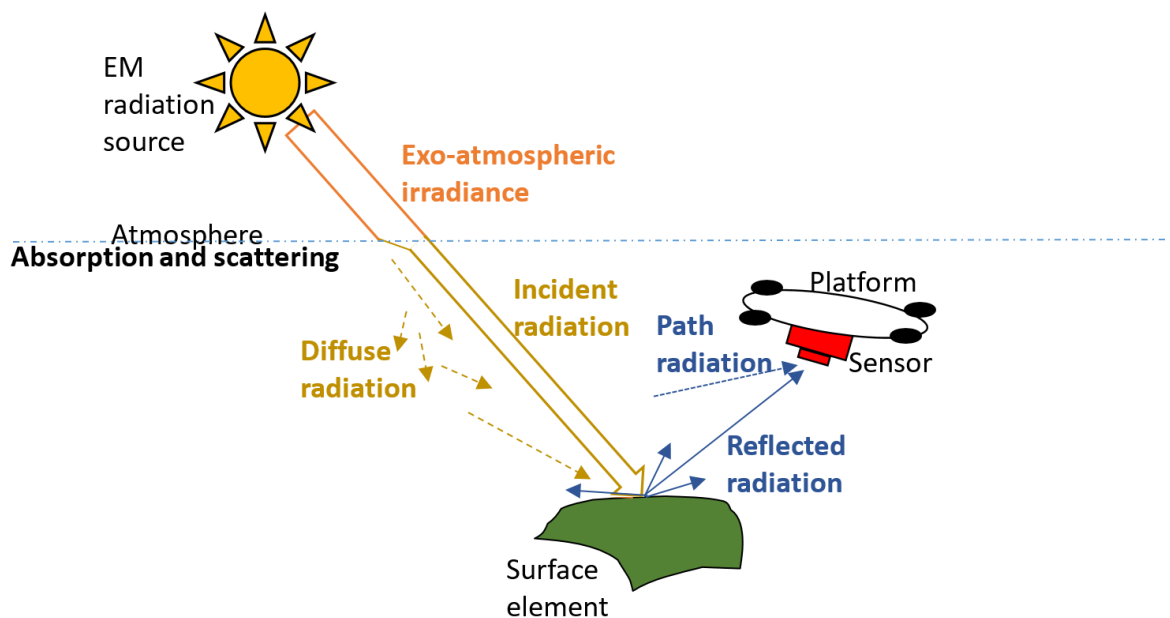


**Figure 2** Simplified radiance diagram for an optical sensor -mounted in a low flying altitude platform.

Radiometric calibration is specially needed when comparing datasets collected during multiple time periods, across sensors or when there are different illumination conditions over the same area. The last one is particularly important when working with UAVs, since the camera takes several images that will be overlapped to generate an orthomosaic (Mitchell 2010; Wang and Myint 2015).

Focusing on UAV imagery, some factors that contribute to radiometric issues are: (1) the use of wide field of view (FOV) imaging equipment that creates an inherent radial variation in viewing angle, (2) the solar motion that creates a non-static illumination source, and (3) even though multispectral UAV imagery is cloud-free, clouds influence the incoming solar radiation at the surveyed area generating darker spots (Dunford et al. 2009; Liu et al. 2016; Stark et al. 2016). The result is a poor stitching of the overlapping images that will generate a less accurate and non-homogeneous orthomosaic. In the same way, the accuracy of the reflectance estimation, vegetation indices, and classification results is reduced. This problem tends to increase with a larger survey area (Dunford et al. 2009; Mitchell 2010; Wang and Myint 2015).

Radiometric calibration methods can be classified into (1) absolute and (2) relative methods. The absolute methods relate the DN values of the image to the radiance at the ground surface, using sensors during the missions. Relative methods are applied when it is not possible to use additional sensors, working mainly with known features and normalizations (Clemens 2012; Prosa et al. 2013).

It is important to mention that traditional RS has an established radiometric correction process while in UAV technology, a systematic, feasible, and convenient radiometric calibration method has not yet been developed (Clemens 2012; Wang and Myint 2015). This study tries to reduce this knowledge gap.

In general, the radiometric calibration process in RS involves:

**(1) Reduction of vignetting effect:**

The vignetting effect consists of the radial fall of brightness from the principal point of the image. It depends on the sensor sensitivity. The vignetting effect can be produced by different physical causes: natural vignetting (due to geometric optics: angle at which the light exits from the rear of the lens), pixel vignetting (due to the angular sensitivity of digital optics), optical vignetting (due to the light path blocked inside the lens body by the lens diaphragm, easily observed by the changing shape of the clear aperture of the lens, which reduces the amount of light reaching the image plane) and mechanical

vignetting (due to certain light path becoming blocked by other camera elements). However, a single polynomial function or a Fourier analysis can reduce this effect (Japan Association of Remote Sensing 1996; Clemens 2012; Prosa et al. 2013; Micasense 2015).

## **(2) Dark current compensation**

The dark current is an effect caused by thermal stimulation of electrons in solid state sensors. It usually adds a pattern on the sensor. To reduce this effect, an image with the lens covered it is taken and subtracted to all the obtained images (Pix4D 2017).

## **(3) Reflectance correction:**

Reflectance is the fraction of incident EM radiation reflected by the analyzed surface. Its values depend on the sun azimuth, surface reflection, topography and illumination (Clemens 2012). Reflectance values are especially important when working with an orthomosaic quantitatively. However, UAV optical sensors register DN values instead of reflectance. For this reason, reflectance correction should be performed. Unfortunately, consumer-grade digital camera manufacturers usually do not provide sensor or spectral band information, making the reflectance correction process difficult (Clemens 2012; Markelin 2013).

In natural conditions most of the objects have anisotropic properties, producing different reflectance effects. The most frequent one is the bidirectional reflectance distribution function (BRDF), which describes the dependence of the object reflectance as a function of illumination and observation geometries. BRDF is difficult to quantify since the reflectance factor of a target surface needs to be measured using a goniospectrometer under equal illumination conditions. The correction of this effect consist of the reduction of the influence of the object reflectance anisotropy by using a class-specific correction function (Markelin 2013; Honkavaara 2014).

## **(4) Atmospheric correction:**

The atmospheric effects depend on the flying altitude and the characteristics of the study area. The atmosphere influence is caused by scattering and gaseous absorption. The types of scattering are: (1) Rayleigh scattering (when the particles are smaller than the light wavelength), (2) Mie scattering (when the particles are of approximately the size of the light wavelength) and (3) nonselective scattering (when

the particles are greater than the light wavelength). The gaseous absorption is primarily due to water vapor, carbon dioxide and oxygen (Honkavaara 2014; Lillesand and Kiefer 2014).

The atmospheric correction is generally omitted due to the low flying height of UAVs. However, in some cases where the amount of aerosols or haze is high, aerosol sensors could be used, like in Zarco-Tejada et al. (2013) or a layered scattering physical-based model could be applied like in Huang et al. (2016).

## 2.4. Vegetation indices

Vegetation indices (VI) combine surface reflectance of two or more spectral bands to study different characteristics of vegetation and to allow inter-comparison (Silleos et al. 2006; Salamí et al. 2014). The Index database (The IDB Project 2017) stores more than 150 VIs, but only some of them are regularly used. Salamí et. al (2014) reported that 21 types of VI have been used with UAV imagery from 1997 until 2014. Table 2 lists the thermal and spectral indices that are most commonly reported in UAV-based remote sensing studies, five of them were selected for this study and they will be presented in the methodology section.

VIs are extensively used for tracing and monitoring vegetation. Some examples are detection of growth levels, water and nutrients stress, yield production, among others. Unfortunately, their quality and confidence are affected by radiometric variations. Chlorophyll and structural indices are usually sensitive to light changes and variations on the sun angle (Silleos et al. 2006; Markelin 2013; Salamí et al. 2014).

**Table 2** Primary vegetation indices used in UAV-based remote sensing

Index	Description	Equation	Reference
<b>Thermal indices</b>			
CWSI	Crop Water Stress Index	$CWSI = (T_{plant} - T_{wet}) / (T_{dry} - T_{wet})$	Jackson et al. (1981)
I <sub>g</sub>	Stomatal Conductance index	$I_g = (T_{dry} - T_{plant}) / (T_{plant} - T_{wet})$	Jones (1999)
<b>Chlorophyll indices</b>			
TCARI	Transformed Chlorophyll Absorption in Reflectance Index	$TCARI = 3[(Re - R) - 0.2 * (Re - G) * (Re/R)]$	Haboudane et al. (2002)
TCARI/OSAVI	Transformed Chlorophyll Absorption in Reflectance/Optimized Soil-Adjusted VI	$TCARI/OSAVI = \frac{3[(Re - R) - 0.2 * (Re - G) * (Re/R)]}{[(1 + 0.16) * (NIR - R) / (NIR + R + 0.16)]}$	Haboudane et al. (2002)
TVI	Triangular Vegetation Index	$TVI = 0.5 * [120 * (Re - G) - 200 * (R - G)]$	Broge and Leblanc (2000)
<b>Xanthophyll indices</b>			
PRI (570)	Photochemical Reflectance Index	$PRI_{570} = (B_{570} - B_{531}) / (B_{570} + B_{531})$	Gamon et al. (1992)
<b>Green/red ratio indices</b>			
GI	Greenness Index	$G_i = G/R$	Smith et al. (1995)
Vigreen	Normalized Difference of green/red	$Vlg = (G - R) / (G + R)$	Gitelson et al. (2002)
<b>Structural indices</b>			
NDVI	Normalized Difference Vegetation Index	$NDVI = (NIR - R) / (NIR + R)$	Rouse et al. (1974)
GNDVI	Green Normalized Difference VI	$GNDVI = (NIR - G) / (NIR + G)$	Gitelson et al. (1996)
RDVI	Renormalized Difference VI	$RDVI = (NIR - R) / (NIR + R)^{0.5}$	Rougean and Breon (1995)
EVI	Enhanced Vegetation Index	$EVI = 2.5 * (NIR - R) / (NIR + 6R - 7.5B + 1)$	Huete et al. (2002)
SAVI	Soil-Adjusted Vegetation Index	$SAVI = (1 + L)(NIR - R) / (NIR + R + L)$	Huete (1988)
MTVI1	Modified Triangular Vegetation Index 1	$MTVI1 = 1.2 * [1.2 * (NIR - G) - 2.5 * (R - G)]$	Broge and Leblanc (2000)
MCARI2	Modified Chlorophyll Absorption Ratio Index 2	$MCARI2 = \frac{1.5 * [2.5 * (NIR - R) - 1.3 * (NIR - G)]}{\sqrt{(2 + NIR + 1)^2 * (6 * NIR - 5 * \sqrt{R})} - 0.5}$	Haboudane et al. (2004)

## 3. Methodology

### 3.1. Study area

The UAV missions took place in two land use areas: a mire and an agricultural field. They belong to the Swedish Infrastructure for Ecosystem Science (SITES). They were selected because the areas are limited and they have small vegetation canopies, which facilitates the research (see Figure 3).

The agricultural area is located at the Lönnstorp Research Station, 12 km northeast of Malmö in south-western Sweden (55°39' N, 13°06' E). The crops under study were sugar beet (*Beta vulgaris* var. *altissima*) and winter rye (*Secale cereale*), with a canopy height of 0.13m in average. For more information visit: <https://www.slu.se/en/departments/biosystems-technology/research-facilites/Lönnstorp/>.

The Mycklemossen mire is located at the Skogaryd Research Catchment, 100 km north of Gothenburg in south-western Sweden (58°22'N, 12°09'E). The dominant species are *Sphagnum rubellum* and *Sphagnum tenellum*, with a canopy height of 0.3 m in average. The peat layers are 6 m deep. Some areas have postglacial deposits on a shallow bedrock, where the soil depth is 0.5–1 m at higher elevations (Walling, 2015). For more information, visit: <http://gvc.gu.se/english/research/skogaryd>.



**Figure 3** Study area a) Mycklemossen mire, b) Lönnstorp agricultural area

### 3.2. UAV characteristics

The missions were conducted using a multispectral camera “MicaSense Rededge” on board of an “Explorian 8” UAV.

#### 3.2.1. Explorian 8 UAV

The UAV platform was a rotary-wing aircraft (quadcopter) with up to 37 min endurance at 3.5 kg take-off weight (TOW) and 20-minute endurance at 6.5 kg TOW (Pitchup AB, Sweden). Some specifications are described in Table 3. The ground control station and the UAV were radio linked, transmitting position, altitude, and status data at 2.4 GHz frequency.

**Table 3** Explorian 8 specifications.

<b>Propulsion system</b>	Four 22.2 V brushless electric motors.
<b>Propellers</b>	Four carbon fiber propellers of 45 cm each.
<b>Energy provider</b>	One 24.0 V (22000 mA) battery.
<b>Height</b>	85 cm
<b>Width</b>	85 cm, 100 cm when propellers expanded.
<b>Maximum TOW</b>	7 Kg
<b>Max speed</b>	13.88 m/s
<b>Controller</b>	FrSky Remote control of 500 m radius

Source: Pitchup AB (2015)

#### 3.2.2. Payload

The Explorian 8 payload consist of an accelerometer, gyroscope, GPS, compass, air telemetry module, data logger, downwelling light sensor (DLS), RGB camera, multispectral camera and thermal camera. Some specifications are presented in Table 4. Even though the three cameras were mounted on the Explorian during the flights, only the multispectral images were used for this study.

**Table 4** Specifications of the sensor used

Camera type	Multispectral
Name	Micasense RedEdge
Focal length (mm)	5.5
HFOV (°)	47.2
Spectral bands	5
Spectral range (nm)	465 – 727
Size dimensions (mm)	120.9 x 65.8 x 46.0
Image size (pixel)	1280 x 960
Bit depth	12-16-bit
Image format	RAW/TIFF
Weight (Kg)	0.15

**Source:** MicaSense (2015)

The multispectral camera is a five band Micasense Rededge camera. It can acquire Red (R), Green (G), Blue (B), Red edge (Re) and Near Infrared (NIR) bands simultaneously (Table 5 and Figure 4). The ground Sample distance is 8.2 cm/pixel per band at 120 m AGL. The camera is powered by the UAV batteries and it provides geo-tagged images.

**Table 5** Spectral information of the MicaSense RedEdge camera

Band Number	Band Name	Center Wavelength (nm)	Bandwidth FWHM (nm)	Range (nm)
1	Blue	475	20	465-485
2	Green	560	20	550-570
3	Red	668	10	663-673
4	NIR	840	40	820-860
5	Red Edge	717	10	712-722

**Source:** Micasense (2015)

The Downwelling Light sensor (DLS) is a 5-band light sensor connected to the Micasense Rededge camera and to the GPS of the UAV. It is mounted on the top of the Explorian 8, facing the sky. It contains a light diffuser that provides an irradiance reference value for each spectral band in  $W/m^2/nm$ . It also has a

magnetometer, providing the measured orientation of the DLS in degrees (irradiance yaw, pitch, and roll). The information is available in the metadata of the pictures captured by the camera (Micasense 2016).

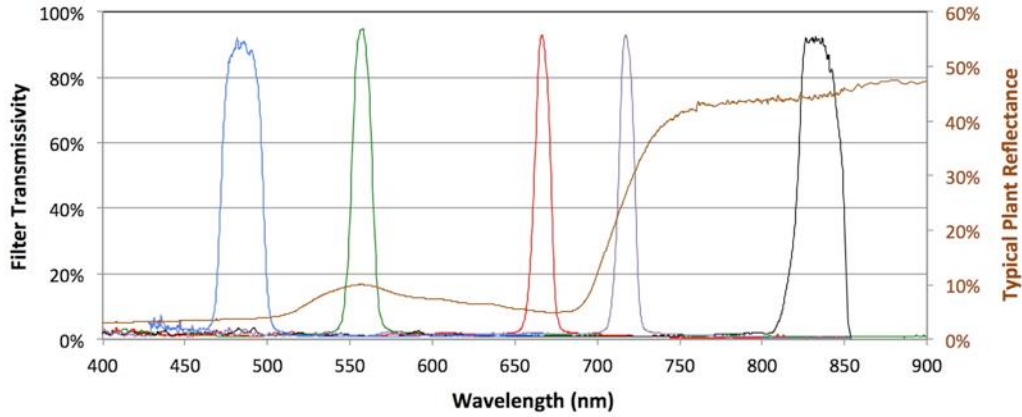


**Figure 4** Spectral response curve for the Micasense RedEdge camera. The colors of the lines correspond to the camera bands. The brown line is a standard reflectance profile of a green vegetation canopy. Source: Micasense (2015)

### 3.3. Software characteristics

As previously mentioned, there are different software packages that can perform SFM. To process Micasense Rededge imagery, the most common are Pix4D, Agisoft PhotoScan Pro and Atlas.

Pix4D mapper is a desktop + cloud software developed by the Swiss company Pix4D. It is an advanced photogrammetry software that uses images to generate radiometric calibrated orthomosaics and 3D spatial data (Pix4D 2017).

Atlas is a cloud-based portal developed by the United States company Micasense. It is designed for processing, management, analytics, and presentation of data captured with MicaSense RedEdge and Parrot Sequoia cameras (Micasense 2017).

Agisoft PhotoScan Pro is a stand-alone software developed by the Russian company Agisoft LLC. It performs photogrammetric processing of digital images and generates 3D spatial data to be used in GIS applications, cultural heritage documentation, and visual effects production as well as for indirect measurements of objects of various scales (Agisoft LLC 2016).

The three software were tested, but only Agisoft PhotoScan Pro and Atlas were selected for this study (Figure 5). According to Micasense (2015), Atlas is the best option to generate Micasense Rededge products, since the cloud software belongs to the camera manufacturer.

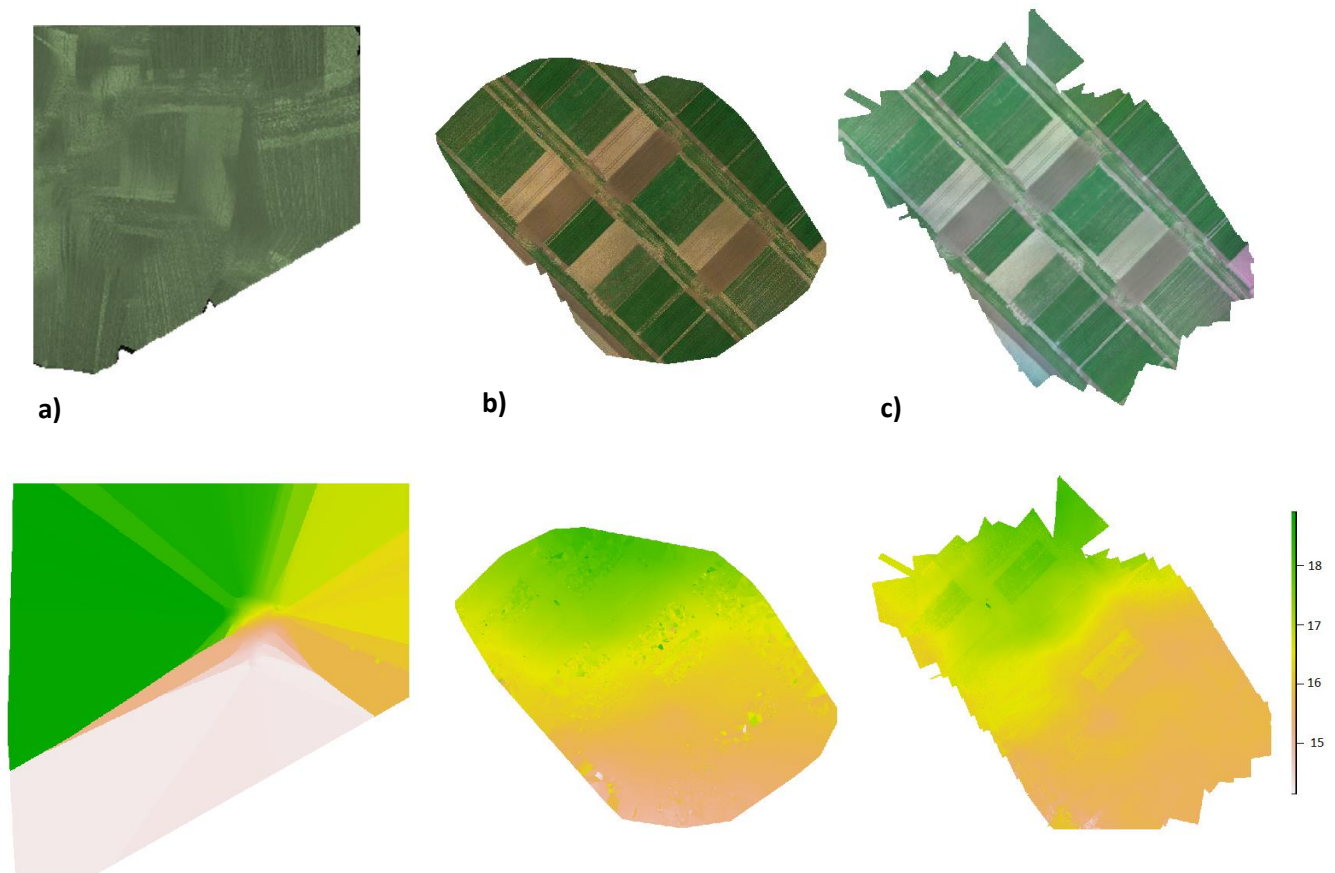


**Figure 5** RGB orthomosaic and DSM generated on a) Pix4D mapper, b) Atlas and c) Agisoft PhotoScan Pro for the same mission in Lönnstorp.

The processes related to the radiometric correction were performed using the software R v.3.3.2. R is an open-source programming language and software environment commonly used in research fields for statistical computing and graphics. It is supported by the R Foundation for Statistical computing. R is a GNU package. The source code for the R software environment is written primarily in C, Fortran, and R. R is freely available under the GNU General Public License (The R Foundation 2017).

All the scripts generated for this thesis can be found on Github (<https://github.com/xime377/RedEdge-calibration.git>).

Since Atlas is a cloud service, uploading the flight images and pictures of the reflective targets is the only requirement to generate an orthomosaic with normalized illumination and reflectance values within 24 hours. For this reason, the tasks described in the following section belong to an Agisoft PhotoScan Pro v 1.3.1 workflow.

### 3.4. Method

The UAV image processing comprises two stages: data collection and data processing. They are outlined in detail in the following sections.

Different radiometric correction methods were tested and compared using vegetation indices. The complete workflow is shown in Figure 6.

During the field data collection, on average 2 hours per mission were spent, while in the data processing 4.5 hours were needed to process one mission.

For the data processing, a workstation of 64 Gb of RAM, with a processor Intel® Core™ i7-6800K with CPU of 3.4GHz was used. The radiometric correction, a semi-automatic process, took 1.5 hours while the orthomosaic generation, a semi-automatic process, took around 3 hours.

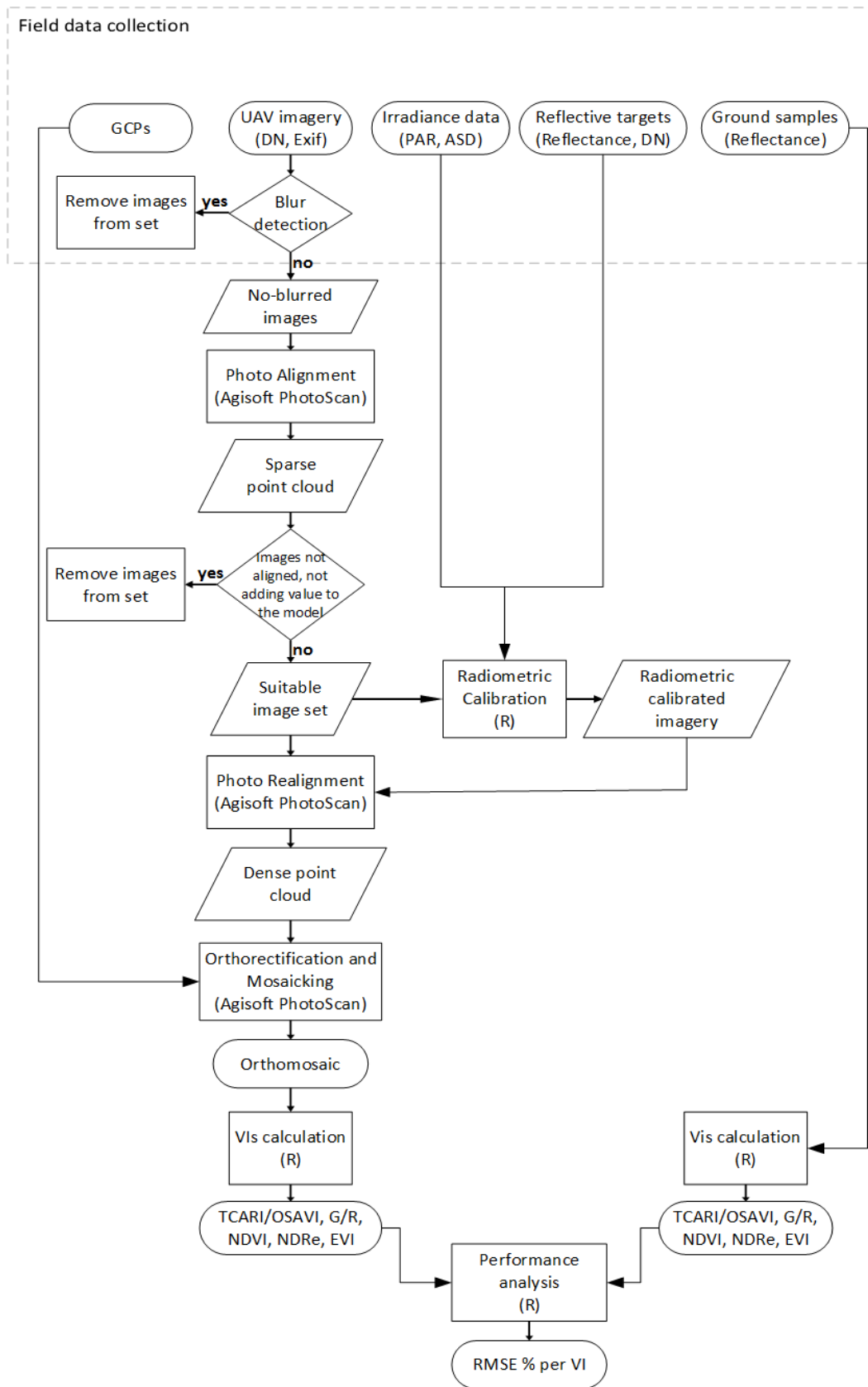


Figure 6 Workflow for processing multispectral UAV imagery to generate a vegetation index map from one UAV mission.

### 3.4.1. Data collection

#### UAV missions

The missions took place from September 2016 to May 2017, under the certificate of authorization number UAS 1B-2274. They were programmed to fly 75 m above the ground station, using the software UgCS (Universal Ground Control Software, SPH Engineering, Latvia). The route pattern was based on the MicaSense camera configuration, having a cross-track and along-track overlap of 80%, see Figure 7. The information of the missions can be found in Table 6.



**Figure 7** Mission planned in UgCS for the agricultural field on Lönnstorp

#### Data log for incident light analysis in UAV imagery

The UAV missions were performed at different times per study area in order to analyze the effects of the variation of solar elevation angle and sky conditions (Majasalmi et al. 2014; Rahman et al. 2014). The sun elevation angle was determined using the National Oceanic and Atmospheric Administration (NOAA) sunrise/sunset and solar position calculator (US Department of Commerce, NOAA 2017). The sky conditions under each mission were registered and classified in three categories related to the presence of clouds: (1) overcast, when the sky is covered in more than 80% by clouds, (2) partly cloudy, when the sky presents less than 80% of clouds and (3) clear sky, when the sky has only few clouds that do not provide much shadows or the sky is free of clouds. Figure 8 shows the three categories found during the missions.



**Figure 8** Pictures of the sky condition classes in Lönnstorp before the flights: a) Overcast, b) Partly cloudy and c) Clear sky.

Data retrieved from The Weather Company LLC (2017)

### Ground measurements

#### - Geometric ground control points

Six target plates of 29 x 29 cm were distributed over the survey area (Figure 9) to be used as ground control points (GCP). Their location was recorded using a Real Time Kinematic (RTK) GPS+GLONASS before the flights.

#### - Reflective targets

Three 50 x 50 cm reflective targets with 10%, 23% and 44% averaged reflectance (MosaicMill, Finland) and two 14.5 x 14.5 cm reflective targets with 55% and 66% averaged reflectance (Micasense, USA) were distributed in the study area as reference for the radiometric correction. They were located level on the ground, in a place without shadowing. A picture of each target was taken using the MicaSense Rededge camera before and after the mission to link the DN<sub>s</sub> with their spectral signatures. The spectral signatures were assessed from different angles (Figure 10) using a hand-held field spectrometer FieldSpec3 ASD (fore-optic, 7.5 FOV), calibrated with a white Spectralon panel of reflectivity near 100%.

#### - Incoming radiation

Incoming radiation data during the time of the mission was obtained using three different sensors: (1) Micasense Downwelling light sensor (DLS), mounted on the UAV; (2) JYP-1000 Photosynthetically active radiation (PAR) sensor, located in the middle of the surveyed area; (3) Field spectrometer FieldSpec3 ASD (fore-optic with a cosine corrector of 180°). All of them were facing the sky.

**Table 6** Information of the UAV missions performed. “S” corresponds to Skogaryd and “L” to Lönnstorp

Mission	Initial time (hh:mm)	Flight time (min)	Coverage area (km <sup>2</sup> )	Camera shutter speed (s)	ISO speed rating	Canopy height (cm)	Solar declination (°)	Solar elevation angle (°)	Sky conditions	Incoming radiation (W/m <sup>2</sup> /nm)*
S_2016-09-16_1	10:00	15	0.02	0.001 - 0.004	100 - 800	30.0	2.41	28.8	Partly cloudy	-
S_2016-09-16_2	10:30	18	0.1	0.001 - 0.012	200 - 800	30.0	2.4	30.98	Partly cloudy	-
S_2016-09-16_3	12:00	24	0.01	0.001 - 0.008	400 - 800	30.0	2.37	34.02	Partly cloudy	-
L_2016-11-03_1	10:47	9	0.06	0.001 - 0.003	200 - 800	10.0	-15.25	17.90	Clear sky	-
L_2016-12-02_1	14:54	9	0.04	0.001 - 0.023	800	10.0	-22.06	3.90	Clear sky	-
L_2016-12-02_2	15:08	9	0.04	0.002 - 0.048	800	10.0	-22.06	2.27	Clear sky	-
L_2017-03-07_1	14:24	8	0.05	0.001 - 0.003	400 - 800	10.0	-5.07	24.03	Overcast	0.24
L_2017-03-13_1	10:32	10	0.07	0.001 - 0.003	400 - 800	10.0	-5.11	28.62	Partly cloudy	-
L_2017-03-13_2	11:55	8.5	0.05	0.001 - 0.002	100 - 800	11.0	-5.11	29.13	Partly cloudy	-
L_2017-03-24_2	13:00	9	0.06	0.0007 - 0.002	100 - 400	12.0	1.59	35.95	Clear sky	0.71
L_2017-04-08_1	11:32:00	9	0.05	0.0006 - 0.002	100 - 800	14.0	7.37	39.06	Overcast	0.30
L_2017-04-08_2	12:10:00	9	0.05	0.001 - 0.002	100 - 800	14.0	7.38	40.94	Overcast	0.31
L_2017-04-30_1	14:37	11	0.06	0.0006 - 0.002	100 - 400	40.0	14.94	44.38	Clear sky	0.98
L_2017-04-30_2	16:49	11	0.06	0.0001 - 0.002	100 - 800	40.0	14.97	29.18	Clear sky	0.42

\*Incoming radiation averaged from the ASD field spectrometer with cosine corrector of 180°.

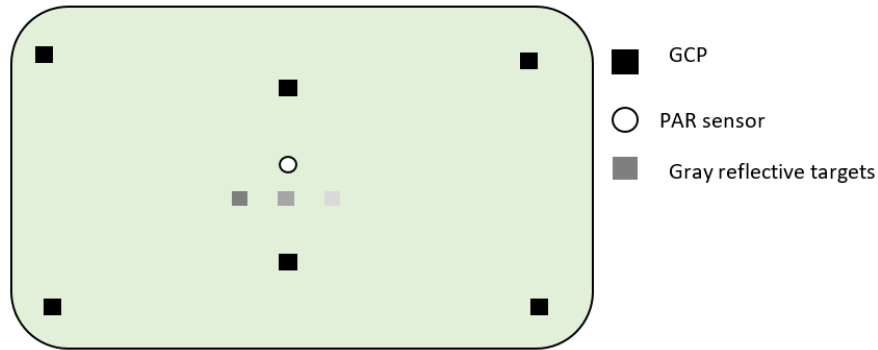


**Figure 9** Targets distribution scheme during a UAV mission. The distribution could vary according to the extent of the mission and the characteristics of the study area.

**- Validation data**

Spectral signatures were assessed per land cover type using a field spectrometer FieldSpec3 ASD (fore-optic, 7.5 FOV, held 0.2 m above the ground from different angle views, having two replicates per angle and 10 replicates per point, see figure 10). The spectrometer was calibrated with a white Spectralon panel of reflectivity near 100%. Two land cover classes were assessed for the validation: (1) bare soil and (2) vegetation. The samples were georeferenced to link them with the correspondent DNs. Ten points were assessed under clear sky conditions and 6 under overcast conditions. It was not possible to assess the 10 points under overcast conditions because it started drizzling during the field work. Figure 11 shows their distribution.

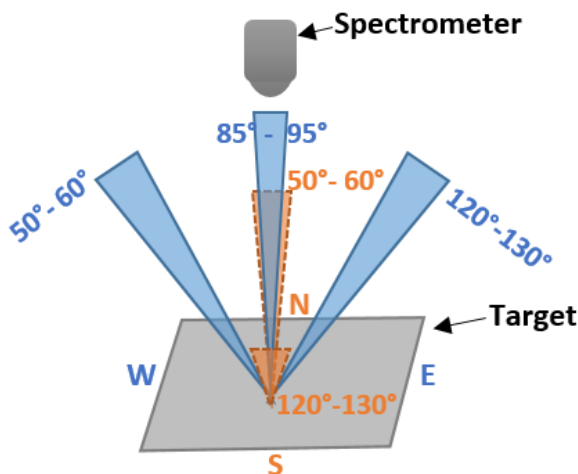


**Figure 10** View angles of the spectrometer during the ground reflectance measurements.

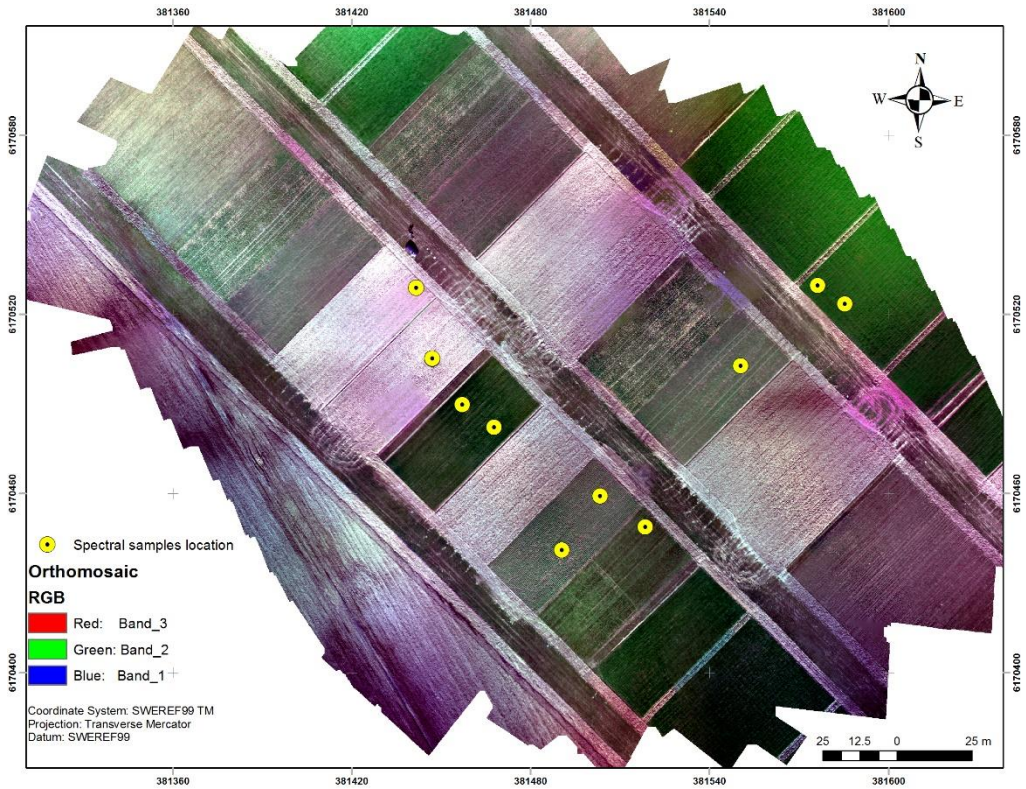


**Figure 11** Map of the validation samples location during the clear sky mission (Lönnpstorp\_24-03-17).

### 3.4.2. Data processing

#### 3.4.2.1 Incident light analysis in UAV imagery

An orthomosaic per mission was generated in Agisoft PhotoScan following the steps described by the USGS National UAS Project Office (2016) to process Micasense Rededge imagery without any radiometric calibration, except the automatically performed by the camera firmware (dark current compensation and reduction of vignetting effect). Fourteen orthomosaics were generated in total.

A visual comparison was performed using all the orthomosaics; however, all the orthomosaics could not be statistically compared since they belong to different dates, having different vegetation growth and soil moisture content. For this reason, only orthomosaics of missions from the same day, with different sun elevation angles, were compared using the Kolmogorov-Smirnov test on the histograms per band. The Kolmogorov-Smirnov distance is a non-parametric test that finds the maximal discrepancy between two histograms (Meshgi and Ishii 2015). The comparison was performed using the `ks.test` function in R v 3.3.2.

A boxplot comparison was made for the orthomosaics of the missions of Lönnstorp 2017-04-30, to see if the variation in the solar elevation angle affects the DN variation of soil, vegetation and reflective targets.

### 3.4.2.2 Radiometric Correction

Different correction methods were tested on each image band prior to the orthomosaic generation. The radiometric calibrated images were used as an input in Agisoft Photoscan to generate an orthomosaic. In all the methods tested, the images had a dark current compensation and reduction of vignetting effect performed automatically by the camera firmware. Table 9 presents the names of the orthomosaics generated using the different radiometric correction methods. In total, nine orthomosaics were produced per mission using Agisoft PhotoScan Pro, and one orthomosaic per mission was generated using the Atlas cloud software.

The correction methods are described in the following section.

**Table 7** Radiometric correction methods compared.

<b>Orthomosaic name</b>	<b>Description</b>
None	Orthomosaic without any radiometric correction except the automatically done by the camera firmware (dark current compensation and vignetting effect).
BC	Orthomosaic generated using brightness correction option from Agisoft Photoscan Pro.
HM	Orthomosaic generated using histogram matching.
SEA	Orthomosaic with only sun elevation angle correction.
ELC	Orthomosaic with only empirical line correction.
EC+ELC	Orthomosaic with exposure compensation and empirical line correction
P+ELC	Orthomosaic with irradiance compensation using PAR data and empirical line correction.
IC+ELC	Orthomosaic with irradiance compensation using DLS data and empirical line correction.
C+SEA	Orthomosaic with IC+ELC and sun elevation angle compensation.
Atlas	Orthomosaic generated in Atlas cloud software.

★ **Dark current compensation**

It is performed automatically by the camera firmware (Pix4D 2017).

★ Reduction of vignetting effect

It is performed automatically by the camera firmware. The coefficients of the equations can be found in RedEdge HTTP Control API (Micasense 2015; Pix4D 2017).

★ Brightness correction - BC

Option available in Agisoft PhotoScan as “Enable color correction”. This option balances the brightness across all the images in the set before generating the orthomosaic, allowing a smooth blending in overlapping areas. This is performed for each image by dividing the brightness value for each band by the total brightness of the image. It does not work well if the contrast is high (Agisoft LLC 2016).

★ Histogram matching - HM

This task was performed on R using the package RStoolbox (Leutner, Horning 2016). The function histMatch performs image to image contrast adjustments based on histogram matching using empirical cumulative distribution functions from both images. The reference image was chosen manually, selecting a central image with small variation between bands.

★ Sun angle correction - SEA

The sun elevation angle was determined using the National Oceanic and Atmospheric Administration (NOAA) sunrise/sunset and solar position calculator (US Department of Commerce, NOAA 2017). This value was used to compensate the images according to Lebourgeois et al. (2008) using the following equation.

$$DN_{SEA} = \frac{DN}{\sin(\alpha)} \quad (1)$$

where  $DN$  is the digital number of the image and  $\alpha$  the solar elevation angle.

★ Exposure Compensation – EC

Lebourgeois (2008) indicated that most researchers use the automated settings on digital cameras. The image analysis can be qualitatively satisfactory, but the radiometric accuracy is usually too low for quantitative surface estimates under the automated settings. Unfortunately, in Micasense Rededge camera it is not possible to change exposure settings directly. It needs to be done through APIs (Micasense 2015). Due to lack of time, the images were taken using automatic settings. However, the exposure compensation performed with the Equation 2 overcomes this issue.

$$DN_{EC} = DN \times \frac{k^2}{\tau K} \quad (2)$$

where  $DN$  is the digital number of the image,  $k$  is the aperture f number,  $\tau$  is the exposure time and  $K$  is the ISO speed (Pix4D 2017).

### ★ Irradiance Compensation

This task was performed in R using different developed methods:

#### *With DLS data - IC*

The irradiance values recorded with the DLS during the flight were extracted from the metadata using the package `exifr` in R (Dunnington and Harvey 2016). They were used to compensate the images by multiplying a correction factor by the DN value of each image, as Hakala et al. (2013) suggest (Equation 3).

However, after several tests, it was noticed that this equation increases the DN values of images with higher irradiance values and it decreases the DN values of images with lower DNs. In the case of Micasense Rededge, the images with lower values are images with less illumination conditions, while brighter images were captured with higher irradiance values. For this reason, an equation that increases the lower DN values and decreases the higher DN values was needed to compensate overcast conditions.

Equation 4 was designed to highlight shadowed areas in missions where the maximum incoming radiance value is lower than  $0.6 \text{ W/m}^2/\text{nm}$  (overcast conditions).

$$DN_{ic} = DN \times (1 - i), \text{ when } i_{max} < 0.6 \quad (3)$$

Equation 4 remains as Hakala et al. (2013) recommended for clear sky conditions, when the maximum incoming radiance value is equal or higher than  $0.6 \text{ W/m}^2/\text{nm}$ .

$$DN_{ic} = DN \times \left(\frac{i}{i_{max}}\right), \text{ when } i_{max} \geq 0.6 \quad (4)$$

where  $DN$  is the digital number of the image,  $i$  is the irradiance correspondent to the image `exif` and  $i_{max}$  the maximum irradiance value of the image set of the mission.

#### *With PAR data - P*

The PAR data was recorded every five seconds providing photon flux density ( $\mu\text{mol/m}^2/\text{s}^1$ ) between the 400 to the 700 nm. This information was linked to the time registered on each picture. Every image was multiplied by a correction factor, following Equations 3 and 4, but using PAR data instead of DLS values.

### ★ Empirical line calibration - ELC

The empirical line method is a common image-based empirical approach for radiometric calibration. It is performed on each sensor band, assuming that there is a relationship between the DN values and the at-surface reflectance, using field spectral measurements to convert the DN values to reflectance

(Lebourgeois et al. 2008; Markelin 2013). For this study, five reflective targets were assessed during different dates, over different light conditions and angles.

- Spectral data of the reflective targets for the ELC

The spectral signatures of the five targets were obtained with the field spectrometer FieldSpec3 ASD (fore-optic, 7.5 FOV); they can be seen in Figure 12.

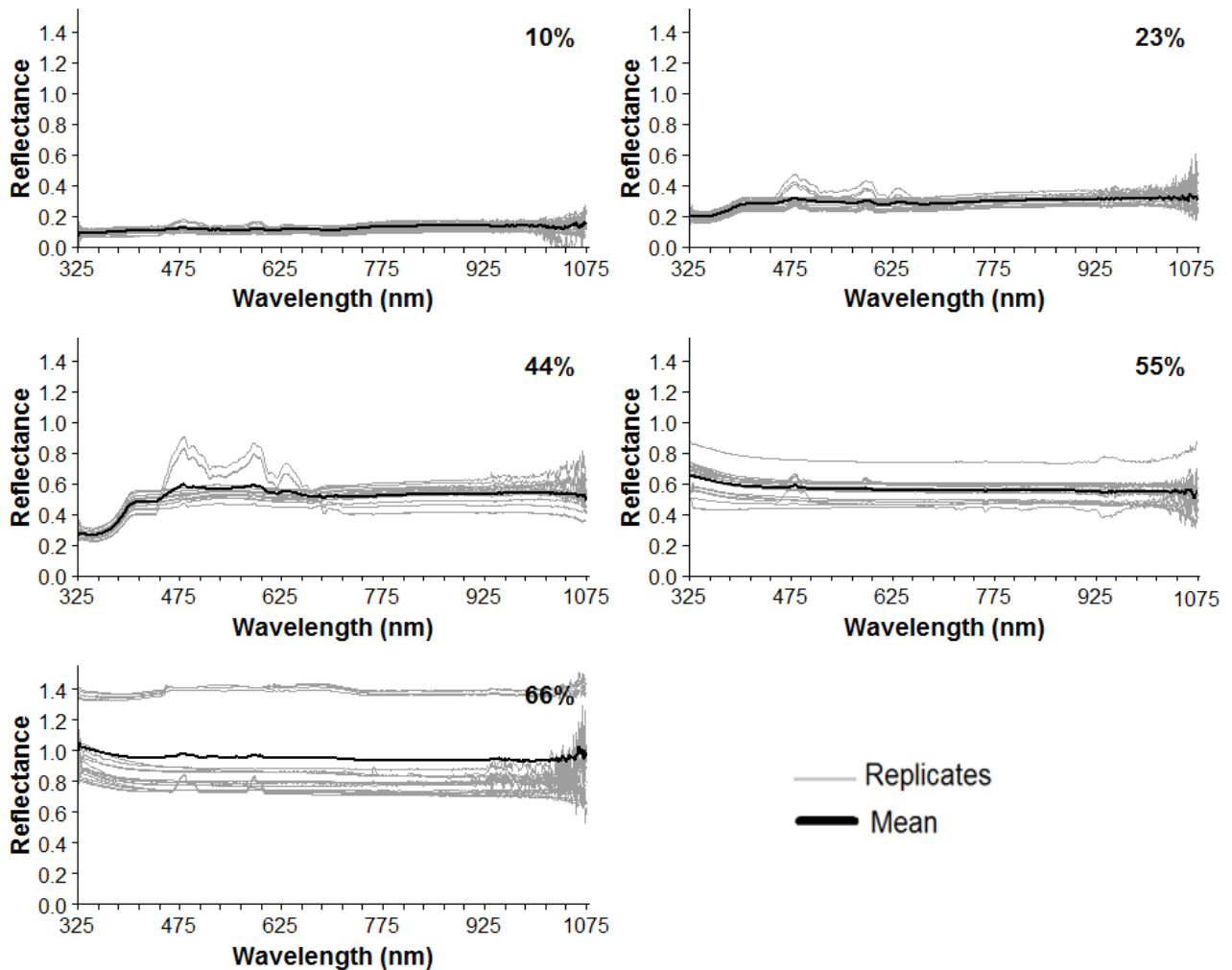


**Figure 12** Spectral signature of 5 reflective targets used for the empirical line calibration. Grey lines are the replicates and the black line is the average.

This data was resampled using a Gaussian Convolution based on a Gaussian kernel following the relative spectral response of each of the MicaSense bands (bell-shaped response curves showed in Figure 4). This process was performed on R, using the package `FieldspectroscopyDP` (Wutzler et al. 2017). The averages can be seen in Table 8.

**Table 8** Reflectance averages per band per reflective target.

Band	Central Wavelength (nm)	Mosaic Mill 10%		Mosaic Mill 23%		Mosaic Mill 44%		MicaSense 55%		MicaSense 66%	
		Mean	Sd	Mean	Sd	mean	Sd	Mean	Sd	mean	Sd
1	475	0.12	0.02	0.31	0.05	0.58	0.12	0.58	0.07	0.81	0.27
2	560	0.11	0.02	0.29	0.04	0.57	0.08	0.56	0.07	0.79	0.28
3	668	0.11	0.02	0.28	0.03	0.51	0.03	0.56	0.07	0.78	0.28
4	840	0.14	0.02	0.30	0.03	0.53	0.06	0.55	0.07	0.77	0.27
5	717	0.11	0.02	0.29	0.03	0.51	0.06	0.55	0.07	0.78	0.28

In order to determine if the targets have Lambertian properties, the samples were tested against:

**Normal distribution:**

The samples per target were assessed using the Shapiro – Wilk’s test (Royston 1982). Where a w value lower than 0.99 and a p-value lower than 0.05 are indicators of a non-normal distribution.

This fact was visually corroborated using Q-Q plots (quantile-quantile plots), where a linear trend is an indicator of normality, while curved trends are indicators of non-normal distribution.

In both cases the results shown a non-normal distribution, Table 8 presents the Shapiro-Wilk’s test results.

**Table 9** Results of the Shapiro-Wilk’s test to determine if the replicates of the spectral measurements have a normal distribution per target.

Target	W	p- value
MM 10%	0.961	0.488
MM 23%	0.922	0.124
MM 44%	0.983	0.985
MS 55%	0.896	0.048
MS 66%	0.699	$5 \times 10^{-5}$

**Analysis of variance**

Since the target samples do not have a normal distribution, the non-parametric Kruskal-Wallis rank sum test was performed to determine if the replicates per target were similar. The distribution of the Kruskal-

Wallis test approximates a chi-square distribution. If the calculated value of Kruskal-Wallis test is greater than the critical chi-square value, at least one of the replicates is different (Hollander and Wolfe 1973).

- DN values of the reflective targets for the ELC:

The pictures of the reflective targets taken at the same moment of the spectral measurements had different exposure settings. In order to work with all the images at the same time, an exposure compensation (EC) was performed using Equation 2.

- Linear regression for the ELC

Once all the images were compensated, the DNs corresponding to the reflective targets were extracted and averaged. The DN average values were linked to their corresponding reflectance value.

According to Pix4D (2017), the Micasense Rededge camera has a linear relationship between DN and reflectance values. For this reason, a linear regression was performed, following Equation 5.

$$Reflectance = m DN + c, \text{ where } m \neq 0 \quad (5)$$

where the constant parameters ( $m$  and  $c$ ) are unique for each band sensor. When the y-intercepts ( $c$  values) are converted to reflectance, they could be interpreted as the minimum possible surface reflectance detected by each sensor band, values that are not influenced by the environmental conditions. For this reason, they could be considered as constant calibration camera parameters (Wang and Myint 2015). Figure 13 shows the results of the regression with the five targets.

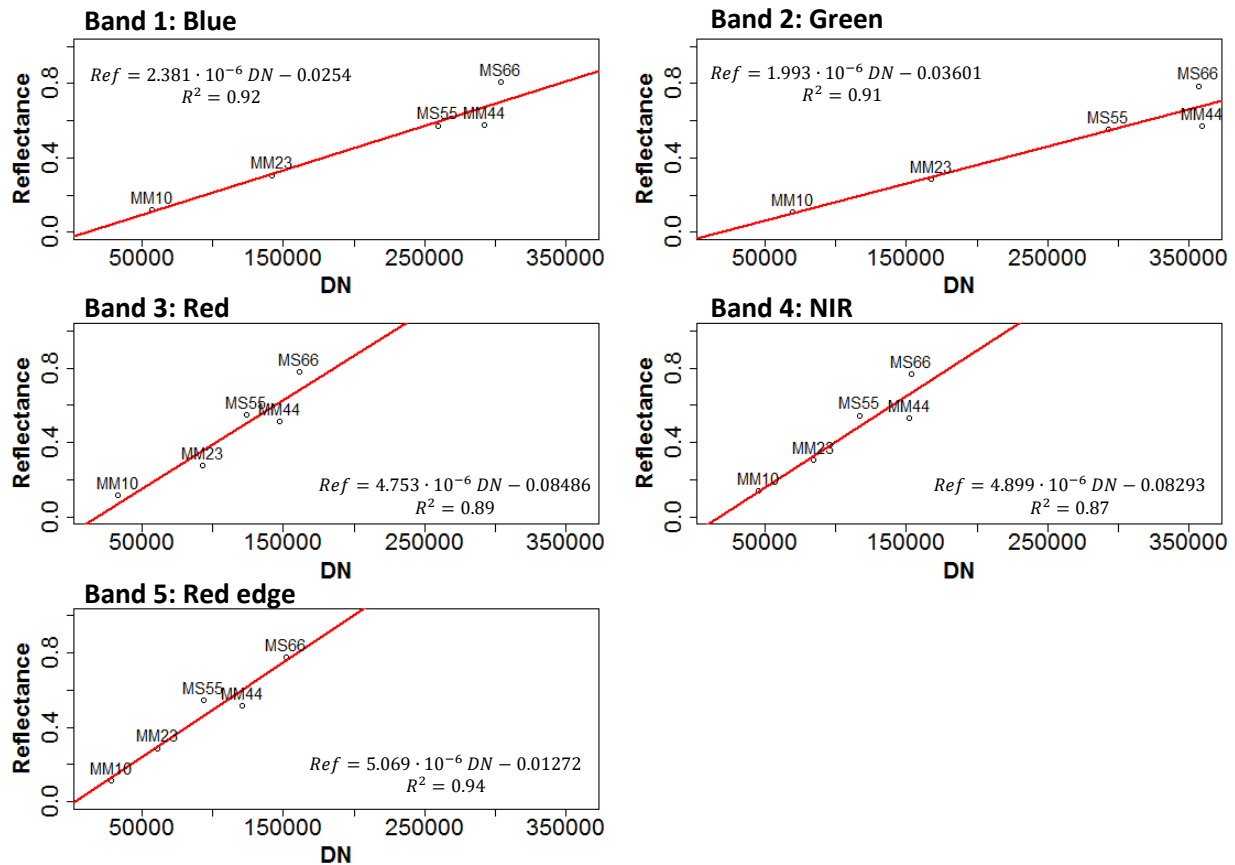


**Figure 13** Linear regression of the ELC with all the reflective targets. MM stands for Mosaic Mill and MS for Micasense reflective targets.

Since the Mosaic Mill target of 44% reflectance had higher values variation and the Cook's distance analysis showed higher distance scores, the target 44% was removed from the regression. This reduced the residual standard error and improved the goodness of fit. Figure 14 shows the linear regression without it.

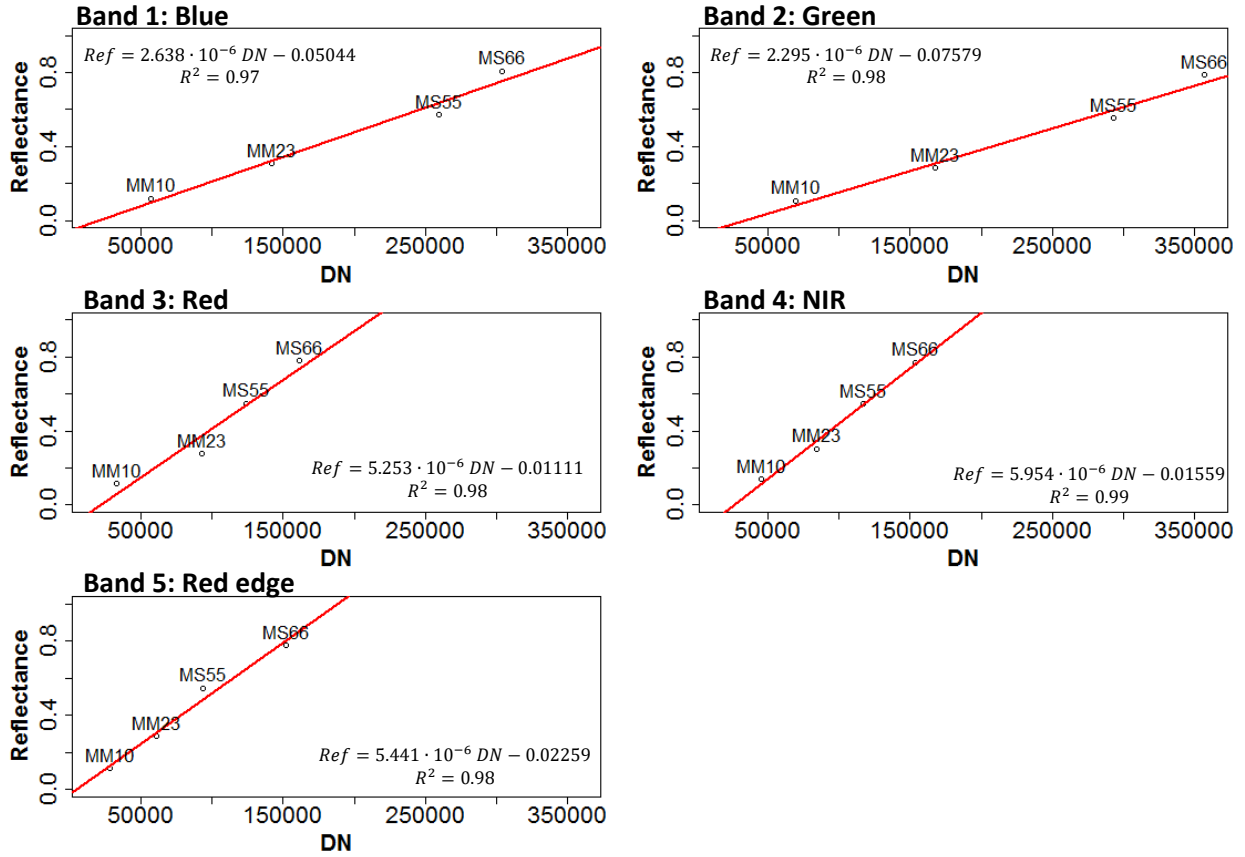


**Figure 14** Linear regression of the ELC with four reflective targets. MM stands for Mosaic Mill and MS for Micasense reflective targets.

Regarding the gain coefficient ( $m$ ), this value will change constantly because the DNs change according to the environmental conditions under the same camera settings (Wang and Myint 2015). For this reason, the gain coefficient was calculated for every mission for each band following Equation 6.

$$m_{band} = \frac{Reflectance_{target} - c}{DN_{target}} \quad (6)$$

where  $Reflectance_{target}$  is the averaged reflectance of the target with less variation per band. In this case is the Mosaic Mill 10% target,  $c$  is the offset determined per band and  $DN_{target}$  is the mean of the digital numbers of the target in the image.

The reflectance values obtained were scaled by 1000 in the orthomosaic to facilitate interpretation.

Unfortunately, it was not possible to apply all the radiometric correction methods in all the orthomosaics due to lack of data for the method, or because time was a limitation. One mission under clear sky (L\_2017-03-24\_2) and one under over cast conditions (L\_2017-04-08\_2) were selected to test the different radiometric correction methods. They are highlighted in Table 9.

Missions before the 13<sup>th</sup> of March do not have Mosaic Mill (MM) reflective targets, for this reason, the ELC was not possible to be performed in those missions. Some missions that have the MM targets do not

have spectral validation samples, thus the performance analysis cannot be done. More details are presented in Table 10, where the collected data and the orthomosaics generated are indicated per mission.

**Table 10** Data collected and orthomosaics generated per mission. The highlighted missions were used for the radiometric correction comparison.

Mission	Data collected						Data processed													
	Ref. targets		I. radiance			Ref.	Cam.	Orthomosaic												
	M S	M M	D L S	P A R	A S D	Val. Sample	EXIF	Pix4D	None	HM	BC	SEA	ELC	EC+ ELC	P+ ELC	IC+ ELC	C+ SEA	Atlas		
S_2016-09-16_1				X			X		X		X									
S_2016-09-16_2				X			X		X		X								X	
S_2016-09-16_3				X			X		X		X									
L_2016-11-03_1	X						X		X		X								X	
L_2016-12-02_1	X						X		X		X								X	
L_2016_12-02_2	X						X		X		X								X	
L_2017-03-07_1	X			X	X	X	X		X		X				X				X	
L_2017-03-13_1		X					X		X		X								X	
L_2017-03-13_2		X					X		X		X								X	
L_2017-03-24_2	X	X	X	X	X	X	X	X	X	X	X	X	X	X		X	X		X	
L_2017-04-08_1			X	X	X		X	X	X		X				X				X	
L_2017-04-08_2	X	X	X	X	X	X	X	X	X	X	X	X	X	X	X	X	X	X	X	
L_2017-04-30_1	X	X	X				X		X		X				X				X	
L_2017-04-30_2	X	X	X				X		X		X								X	

### 3.4.2.3 Vegetation Indices calculation and performance analysis

To evaluate general radiometric quality of the images, a histogram comparison per band was performed on the orthomosaics, followed by a vegetation index performance comparison.

Five of the most common vegetation indices were selected. All the bands of the Micasense Rededge were used in at least one index. The GI, NDVI, NDR<sub>e</sub>, EVI and TCARI vegetation indices were calculated for each orthomosaic generated with a different radiometric correction method. Their equations are shown in Table 11.

**Table 11** Vegetation indices used for the radiometric correction comparison.

The bands are abbreviated as follows: R (Red), G (Green), B (Blue), Re (Red edge), NIR (Near infrared).

Index	Equation	Reference
<b>Chlorophyll index</b>		
TCARI/OSAVI	$TCARI/OSAVI = \frac{3[(Re - R) - 0.2 * (Re - G) * (Re/R)]}{[(1 + 0.16) * (NIR - R)/(NIR + R + 0.16)]}$	Haboudane et al. (2002)
<b>Green/red ratio index</b>		
GI	$G_i = G/R$	Smith et al. (1995)
<b>Structural indices</b>		
NDVI	$NDVI = (NIR - R)/(NIR + R)$	Rouse et al. (1974)
NDR <sub>e</sub>	$NDR_e = (NIR - Re)/(NIR + Re)$	Barnes et al. (2000)
EVI	$EVI = 2.5 * (NIR - R)/(NIR + 6R - 7.5B + 1)$	Huete et al. (2002)

The results of each radiometric correction method were compared against the values of the vegetation indices from the ground spectral data using the percentage root mean square error (RMSE%) (Equation 7).

$$RMSE_{\%} = \sqrt{\frac{\sum_{k=1}^n (E_{\%})^2}{n}}, \text{ where } E_{\%} = \frac{(VI_{method} - VI_{ground\ data}) \times 100}{VI_{ground\ data}} \quad (7)$$

where  $E$  is the error in percentage,  $n$  the number of samples,  $k$  is the index of summation,  $VI_{method}$  is the mean value of the vegetation index pixels 0.3 m surrounding the location of the validation sample.  $VI_{ground\ data}$  is the value of the spectral data collected on the field, resampled on the same way as the reflective targets data.

The comparison was performed on two missions: one under clear sky and one under overcast conditions.

# 4. Results

## 4.1. Incident light variation in UAV imagery

Presence of clouds and solar elevation angle are two factors that cause incident light variations in UAV imagery. Even though UAV imagery is cloud free, the presence of clouds affects the incoming irradiance and the path radiance. Clouds absorb part of the incoming radiation which will be released as diffuse radiation, affecting different wavelengths differently. Figure 15 presents the irradiance measured with the field spectrometer over different sky conditions. As expected, the irradiance at the ground decreases when the presence of clouds increases, having higher values with clear sky and lower values when the sky is overcast.

Comparing the absolute DLS irradiance with the field spectrometer values, it was noticed that the values from the DLS were lower than the values obtained with the spectrometer by 22 to 44%. One example is the mission of the 7<sup>th</sup> of March, first graph of figure 15, where the average irradiance from the ASD is 0.24 W/m<sup>2</sup>/nm, while the DLS sensor provides an average of 0.16 W/m<sup>2</sup>/nm/

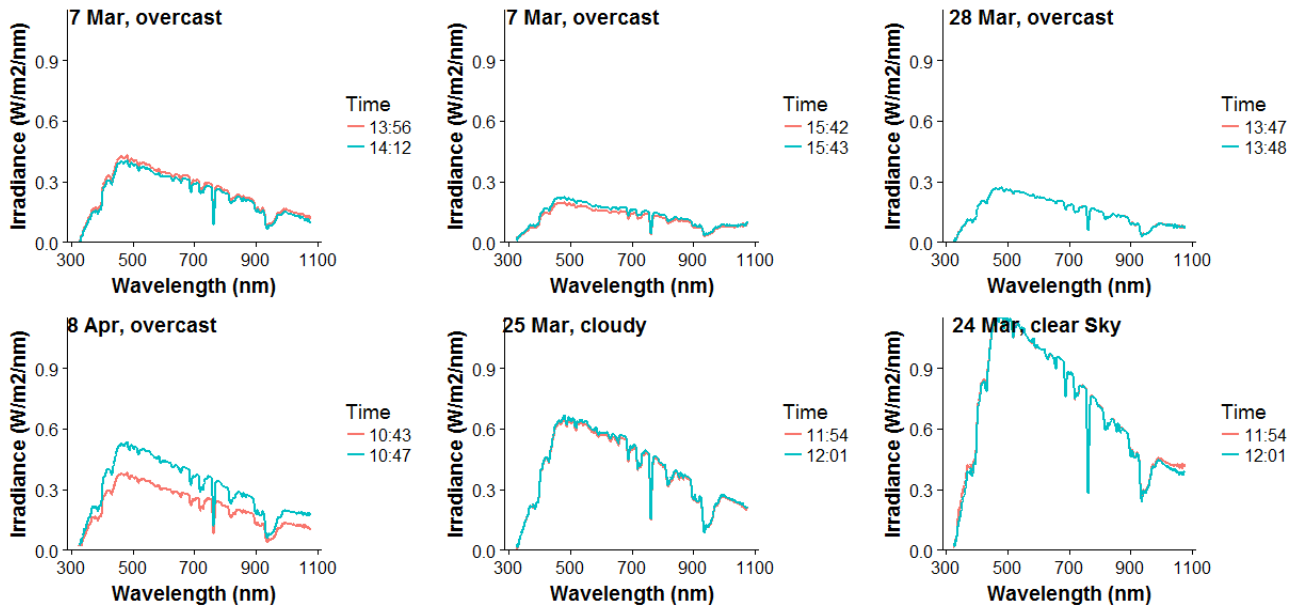


**Figure 15** Irradiance measured at the ground by the field spectrometer with cosine corrector of 180° during different dates and sky conditions.

The difference on the type of radiation affects the reflectance of the objects. When the sky is overcast, diffuse radiation will be predominant, while when the sky is clear, direct radiation will dominate. This affects the reflectance of non-Lambertian objects. Figure 16 shows the variation of the reflectance

measured from different angles of the calibration targets per illumination conditions. The target with least amount of variation regarding the illumination conditions was the Mosaic Mill 10%, while the Mosaic Mill of 44% and the Micasense targets have higher variation. This fact was confirmed with the Kruskal- Wallis test (Table 12), where all the targets got a Chi-squared value higher than the critical Chi-squared, having a p-value lower than  $2.2 \times 10^{-16}$ , which indicates that the spectral measurements of the targets are not similar; hence the targets do not have Lambertian properties. The targets of 44%, 55% and 66% of reflectance have strong bidirectional effects.

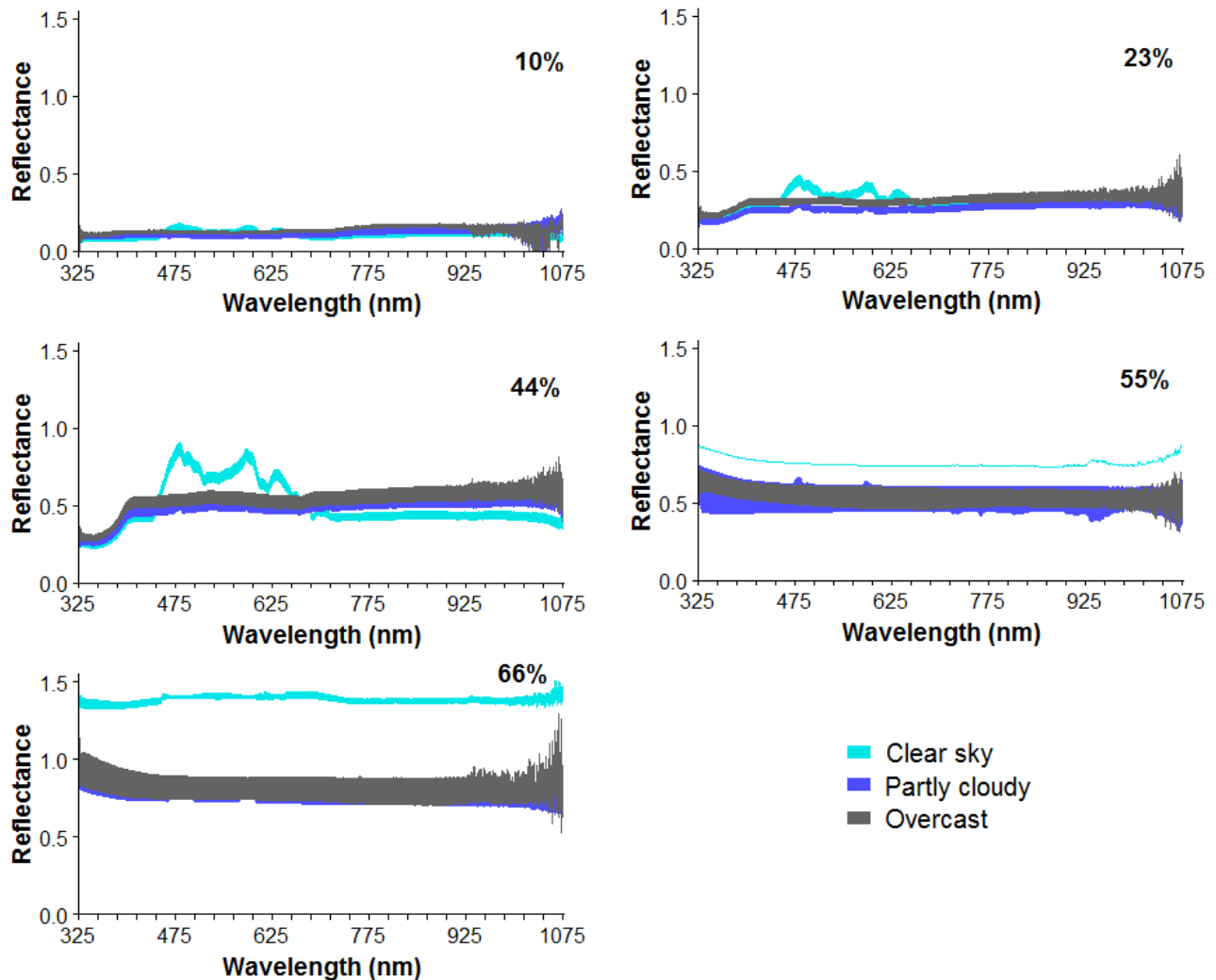


**Figure 16** Reflectance of the calibration targets per illumination conditions.

The high reflectance found during clear sky days corresponds to back scattering, when the BRDF displays its maximum reflectance because the sensor was in direct alignment between the sun and the reflective target.

**Table 12** Results of the Kruskal-Wallis rank sum test to determine the Lambertian properties of the reflective targets.

Target	Degrees of freedom	Chi-squared	Critical	p-value
			Chi-squared ( $\alpha=0.05$ )	
MM 10%	22	5463.1	33.93	$< 2.2 \times 10^{-16}$
MM 23%	18	5894.4	28.87	$< 2.2 \times 10^{-16}$
MM 44%	11	4080.1	19.68	$< 2.2 \times 10^{-16}$
MS 55%	17	6737.9	27.59	$< 2.2 \times 10^{-16}$
MS 66%	13	4810.4	22.36	$< 2.2 \times 10^{-16}$

Solar elevation angle plays an important role at higher latitudes. It varies according to the location, season and time of the day, providing different illumination conditions. When the sun elevation angle is low, the irradiance is lower because the sun energy is spread out over a larger area.

In Table 6 the irradiance values measured at the ground and sun elevation angle of the missions used on this study were presented. There, it is possible to appreciate that the irradiance values increase when the sun elevation angle increases. In addition, the presence of clouds at any sun elevation angle always reduce the irradiance values measured at the ground.

For this reason, a mission with a sun elevation angle of  $44^\circ$  had an irradiance value of  $0.98 \text{ W/m}^2/\text{nm}$  in clear sky conditions, while a mission with a sun elevation angle of  $41^\circ$  had an irradiance value of  $0.31 \text{ W/m}^2/\text{nm}$  when the sky was overcast. The irradiance values were lower when the sun elevation angle was  $24^\circ$  and the sky was overcast, with an irradiance value of  $0.24 \text{ W/m}^2/\text{nm}$ . Figures 17 and 18 present the RGB orthomosaics from Skogaryd and Lönnstorp missions without any radiometric correction, and with different sun elevation angles and sky conditions.

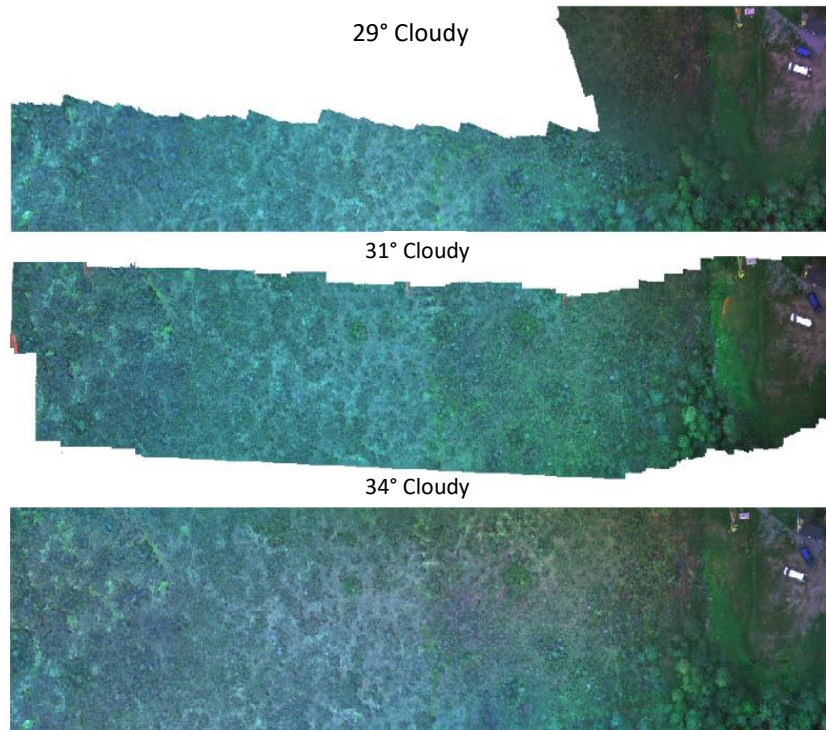


**Figure 17** RGB orthomosaics generated in Agisoft Photoscan without any radiometric correction from Skogaryd missions. They are organized from the lowest sun elevation angle to the highest.

Orthomosaics of missions under overcast conditions are, in general, more homogeneous due to the dominance of diffuse radiation (Figure 18). In the case of missions under cloudy conditions (Figures 17 and 18), the orthomosaics have more presence of shadows because the incoming radiation is not homogenous, the clouds will reduce the incoming radiation in the areas where they are located. On the other hand, the sun elevation angle has more influence on orthomosaics generated from missions under clear sky, since the direct radiation is dominant in this case.

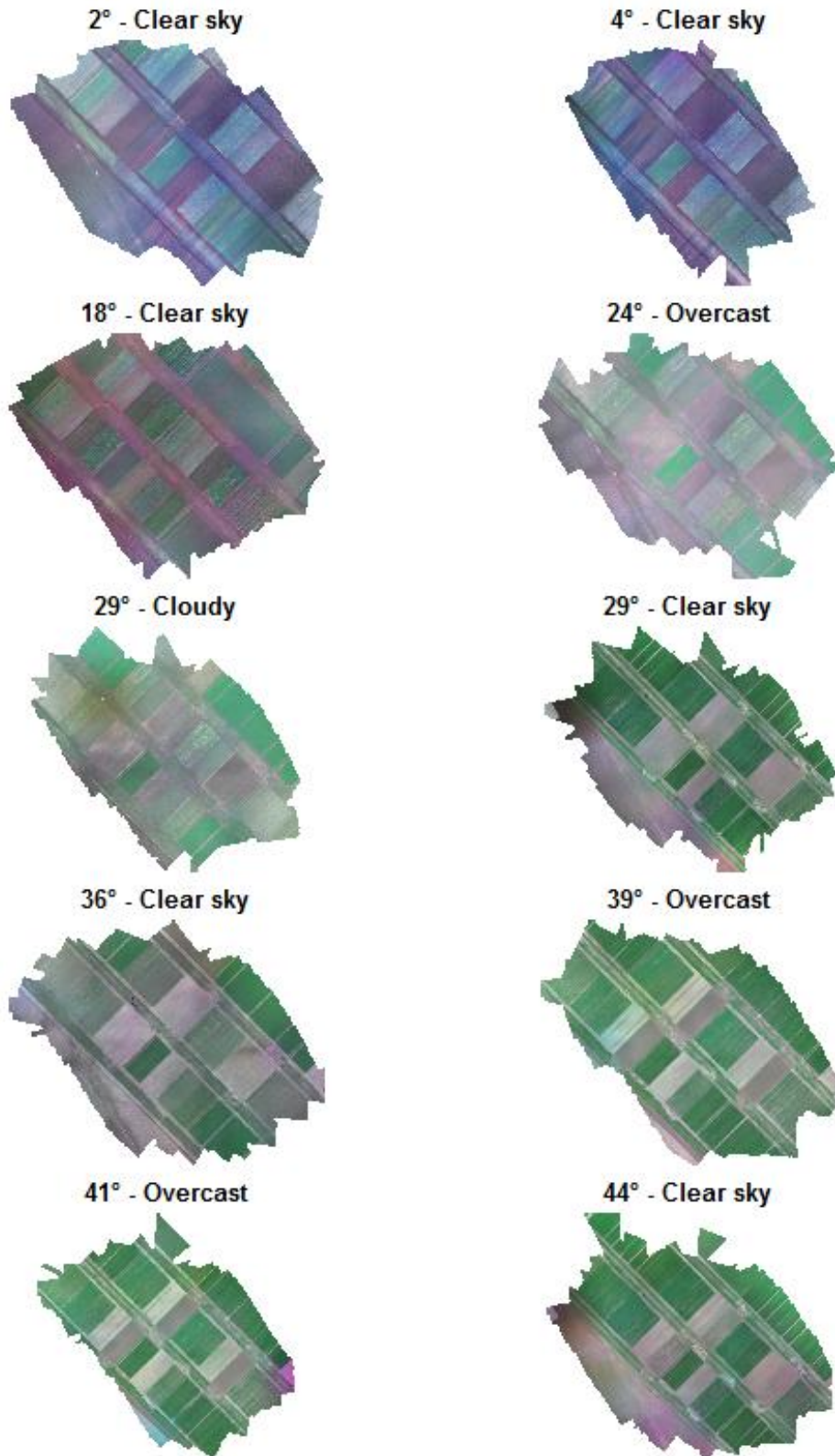


**Figure 18** RGB orthomosaics generated in Agisoft Photoscan without any radiometric correction from Lönnpstorp missions. They are organized from the lowest sun elevation angle to the highest.

The histogram comparison performed to all the bands of each orthomosaic showed that Red band is one of the bands that is more sensitive to the variation of sun elevation angle, while NIR band is the one with less variation with respect to the sun elevation angle. Figure 19 presents the histogram comparison for bands red and NIR of the missions under clear sky Lönnstorp 2017-04-30 with a solar elevation angle of 29 and 44 (Figure 19a), the histogram overlay of the mission under cloudy conditions Skogaryd 2016-09-16 with solar elevation angle of 29, 31 and 34 (Figure 19b); and the histogram comparison under overcast conditions of the missions of Lönnstorp 2017-04-08 with solar elevation angle of 39 and 41 (Figure 19c).

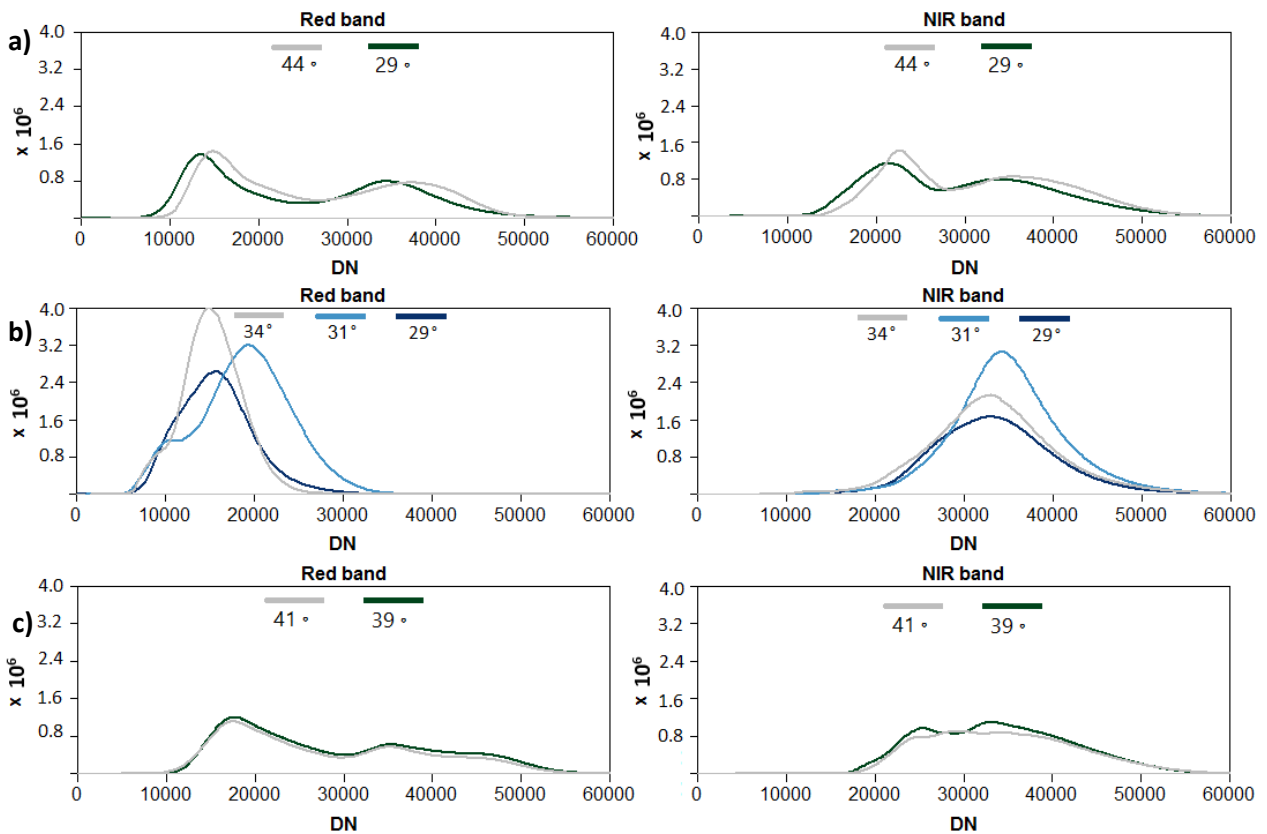


**Figure 19** Overlay of the histograms from the orthomosaics with different sun elevation angles for the red and NIR bands. a) Clear sky in Lönnstorp, b) Partly cloudy sky in Skogaryd, c) Overcast conditions in Lönnstorp.

In Figure 19 it can be seen that under clear sky, the sun elevation has greater impact on the orthomosaics. Nevertheless, this variation can also be found in orthomosaics of missions under overcast conditions, unfortunately the missions under overcast conditions were realized having only 2° of difference, so the difference is not very noticeable (Figure 19c).

Under clear sky conditions (Figure 19a), the orthomosaic of 29° of sun elevation (darker line) have higher frequency of low DN values in all the bands, which indicates the presence of more shadowed areas. The orthomosaic of 44° of sun elevation (lighter line) has a similar distribution but shifted to the right, having lower frequency of low DN values, having orthomosaics with less shadows. The Kolmogorov-Smirnov test against the histograms of the red band gave a D value of 0.05 and a p-value lower than  $2.2 \times 10^{-16}$ , which gives significant statistical difference between the two histograms.

The histograms of the orthomosaics generated under partly cloudy conditions during the same day in Skogaryd have significant variation among them in all the bands, having p-values lower than  $2.2 \times 10^{-16}$ . The differences are mainly in the shapes of the R, G and B histograms with different sun elevation angles. This may be due to a larger amount of shadows when the sun elevation angle is lower, especially in the part that the vegetation canopy is higher. The presence of trees increases the BRDF effect, which is higher at lower sun elevation angles.

Since the histogram analysis was performed for the whole orthomosaic, a boxplot analysis of different features per bands was performed, using the missions under clear sky with 29° and 44° of sun elevation angles. The boxplots of the B, G, R and NIR bands showed that only the beetroot has higher values when the sun elevation angle was 44°, while soil and winter rye do not have much variation. This could be due to the strong BRDF effect that this crop has. The red edge band is more sensitive to the variation of the sun elevation angle, where the beetroot values and the Mosaic Mill 10% reflectance target got higher values when the sun elevation angle was 44°. The boxplots for the NIR and Red edge bands are presented in Figure 20.

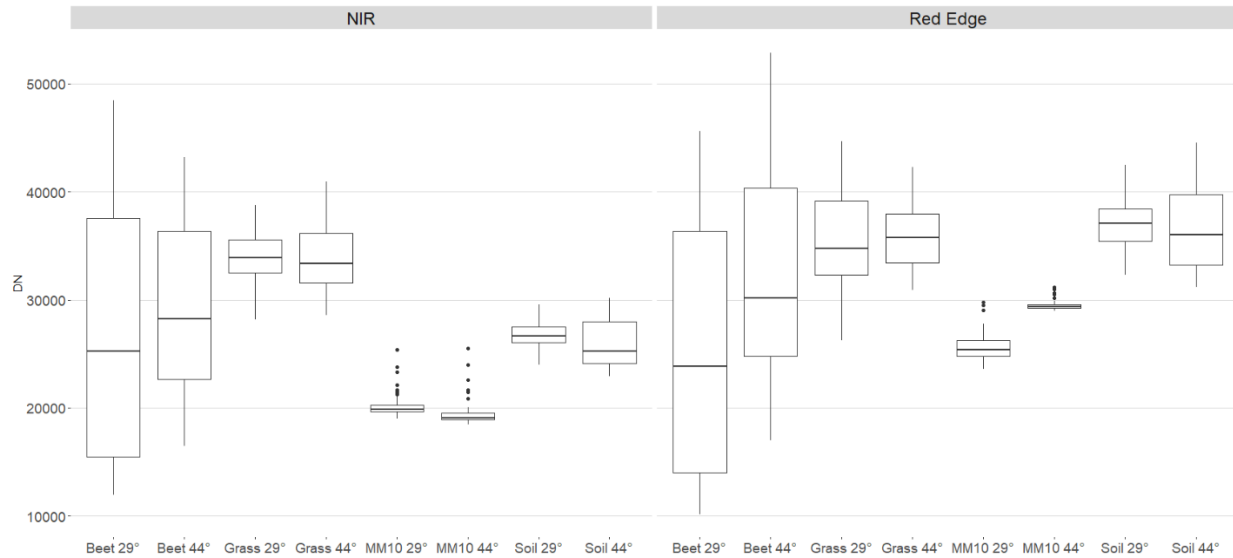


**Figure 20** Boxplot of pixel values of beetroot (*Beet*), MM target of 10% reflectance (*MM10*), soil and winter rye (*Grass*) corresponding to the NIR and Red edge bands of the orthomosaics under 29° and 44° of sun elevation.

## 4.2. Radiometric variations in vegetation indices

As stated in the previous section, illumination conditions affect the UAV imagery. For this reason, the radiometric correction methods were tested in a mission under clear sky and in a mission under overcast conditions. Figures 21 and 22 present the RGB orthomosaics with the correction methods tested.

When compared visually, the orthomosaic generated using brightness correction in the mission under clear sky (Figure 21) does not differ much from the orthomosaic without correction, while in the overcast mission (Figure 22) the brightness correction reduces the color differences on the bottom right corner of the orthomosaic.

The histogram matching showed in both missions that the orthomosaics look brighter and more homogeneous (Figure 21 and 22). The orthomosaics generated using only sun elevation angle correction are darker than the rest of orthomosaics in both cases. However, a quantitative comparison is required to assess the methods performance. The method comparison using vegetation indices is presented in the following section.

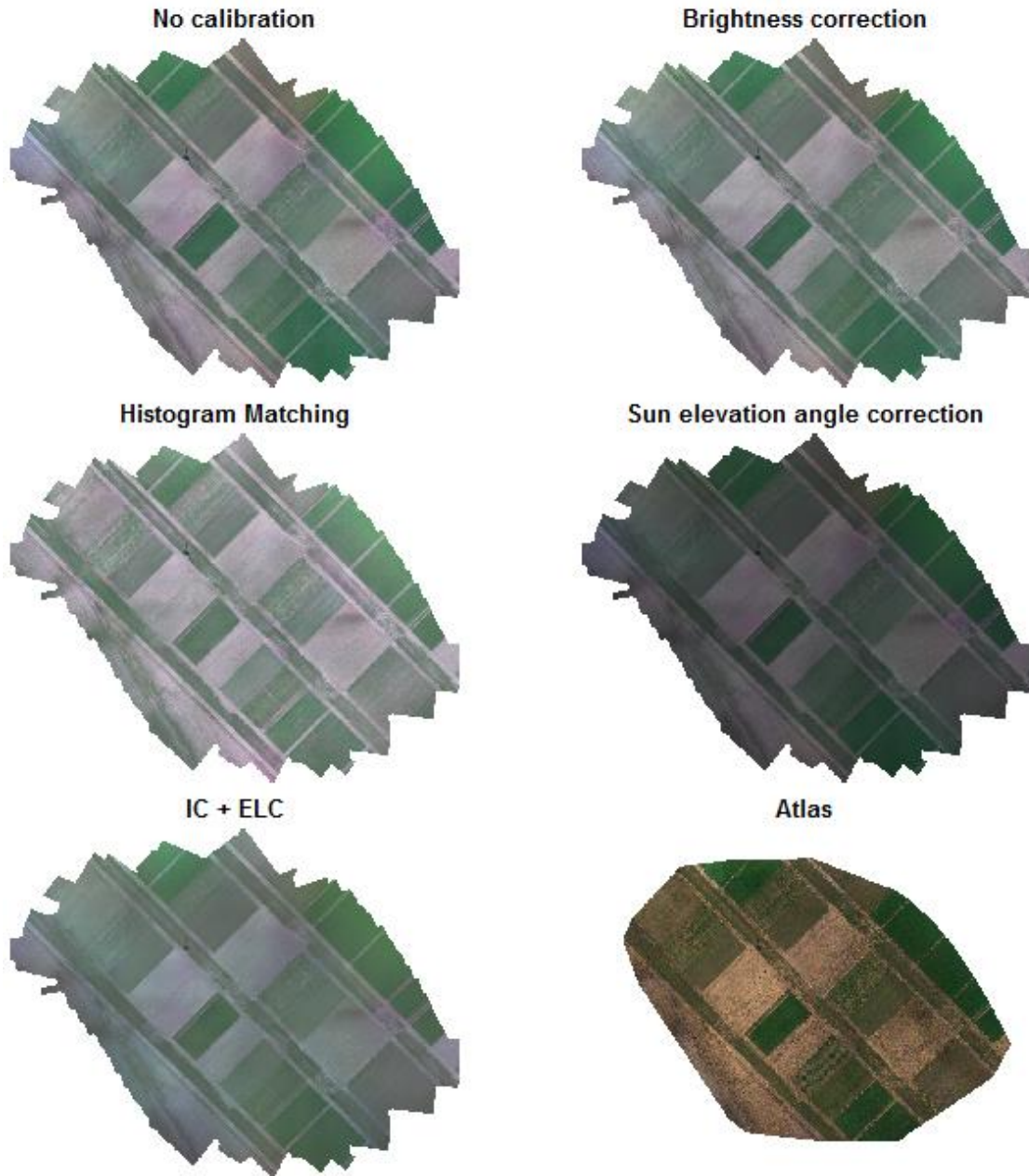


*Figure 21 RGB orthomosaics generated in Agisoft Photoscan with different radiometric correction methods under clear sky conditions (Lönnpstorp 24-03-2017)/ IC+ELC stands for Irradiance Compensation and Empirical Line Calibration.*

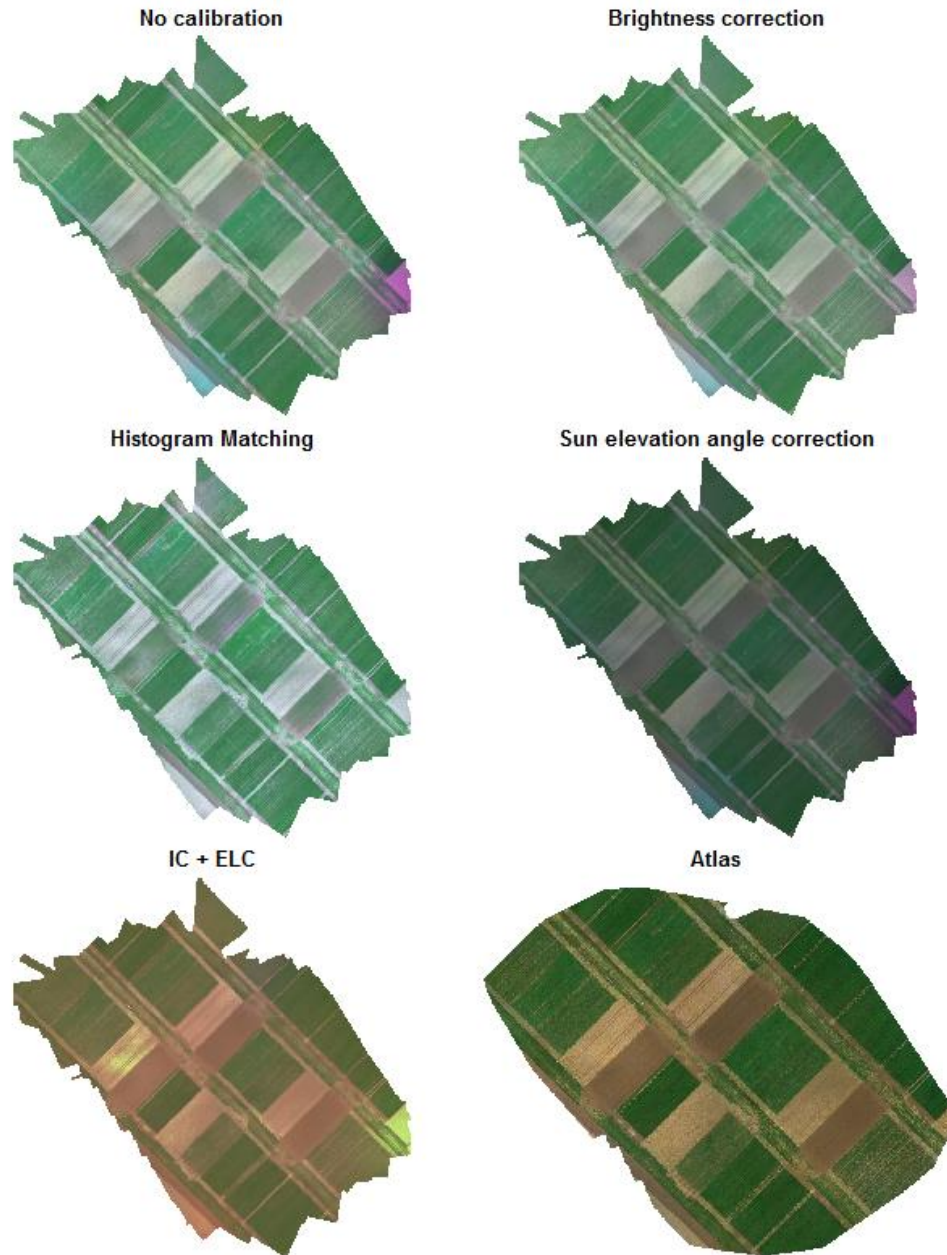


*Figure 22 RGB orthomosaics generated in Agisoft Photoscan with different radiometric correction methods for a mission under overcast conditions (Lönnpö 08-04-2017)*

The histograms of all the bands for each radiometric correction method are shown in Figure 23. Variations of each individual spectral band should be considered to understand the variation of vegetation indices derived from these bands. Since vegetation indices are derived by using two or more bands, in cases where variation in individual bands is not considered the errors are likely to be higher due to error propagation. In the histogram of the orthomosaic without any radiometric correction, the R, G and B bands have similar shape and distribution. Conversely, the Red edge and NIR bands are distinct, however

they still show similar distribution between the two of them. All the bands keep similar distribution when brightness correction is applied. Only red edge band has a small increase of its frequency when histogram matching is applied. This changes in the other radiometric correction methods, where Green and Red edge bands tend to have more of lower DN values compared with the other bands. On the other hand, Atlas software changes all the band distributions, reducing the frequency of the Red edge band.

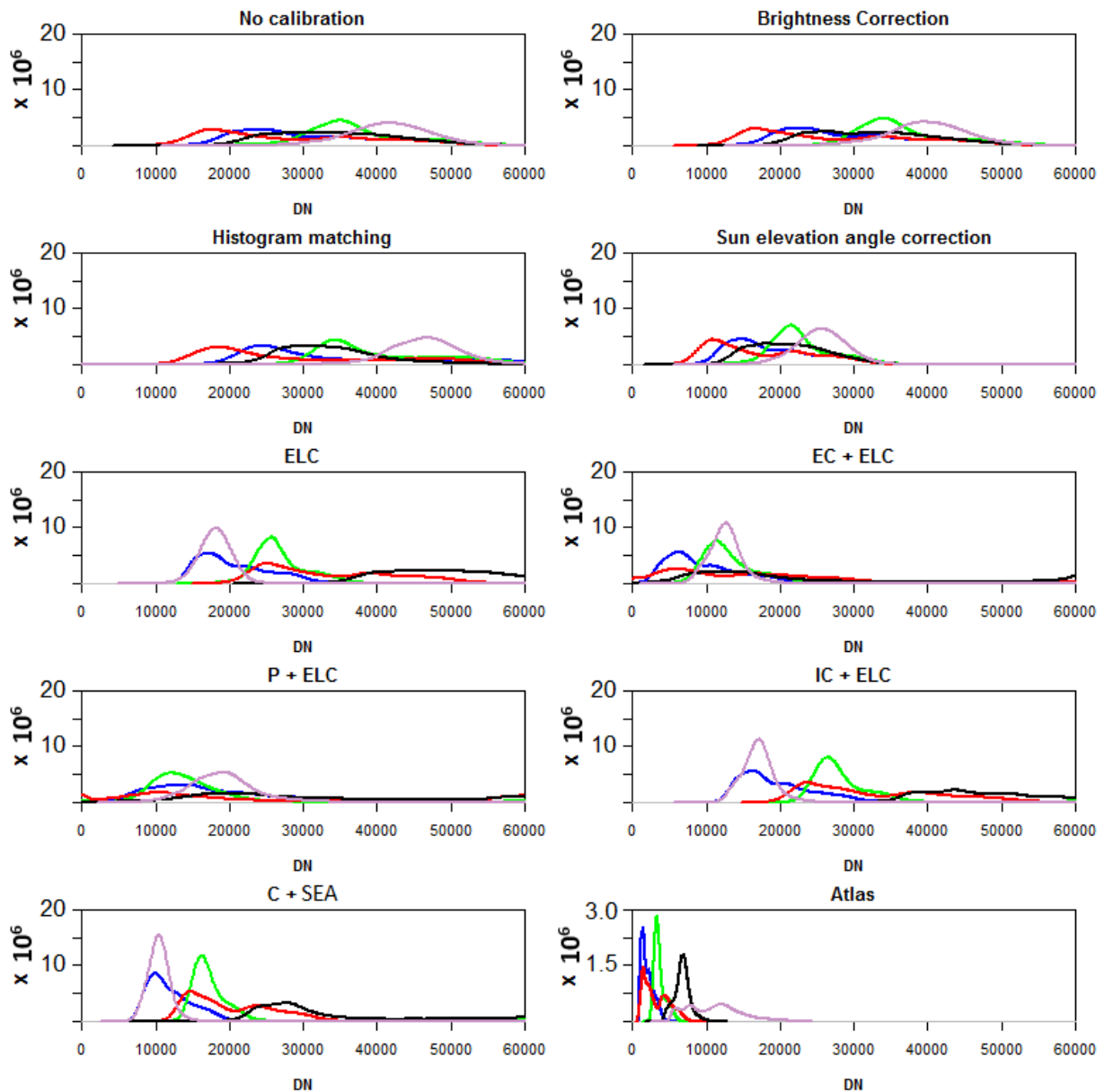


**Figure 23** Histograms of the orthomosaics generated with different radiometric correction methods of the overcast mission (Lönnpstorp 08-04-2017). The colors of the lines correspond to the camera bands. Red: R band, Green: G band, Blue: B band, Black: NIR band, Purple: Red edge band.

### 4.2.1. Chlorophyll index

#### ***TCARI/OSAVI***

The TCARI/OSAVI index calculated from the orthomosaics with different radiometric correction methods is inaccurate in all the cases. The values highly differ from the ground spectral samples. The Percentage RMSE obtained from all the methods tested in the overcast mission were extremely high. The TCARI/OSAVI from the Atlas cloud software was the one with least amount of RMSE with 19378%. The amount of errors of the radiometric correction methods tested on the mission under clear sky are presented in Figure 24. It can be seen that the combination of irradiance compensation, empirical line calibration and sun elevation angle compensation has relatively low error (177%). This is possibly due to the way that the correction methods modify the Red edge and Green bands. Since the index uses the values of Red edge and Green bands in the denominator, which are higher when compared to the other bands, the values of the index will therefore be extremely high.

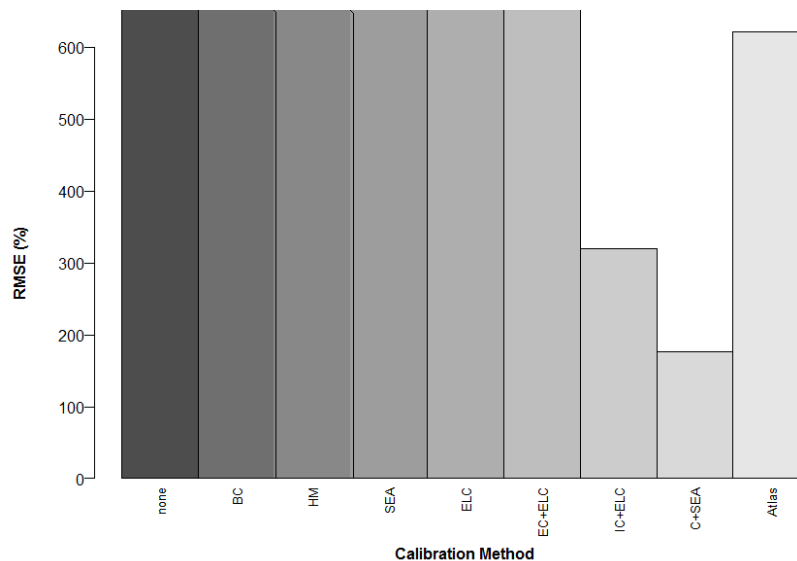


**Figure 24** RMSE statistics (%) for radiometric correction method comparison on TCARI/OSAVI of the clear sky mission.

C+SEA stands for IC+ELC+ Sun elevation angle correction.

### 4.2.2. Green ratio index

#### ***GI***

The GI values obtained from the orthomosaics with different radiometric correction methods of the mission under overcast conditions are close to the ground samples values, except in the case of the P+ELC and EC+ELC, where the RMSE are 87% and 116% respectively. This is caused by the high values assigned to the Red band that are not proportional to the values assigned to the green band (Figure 25). The GI

from Atlas has the lowest RMSE value with 21%. This indicates that the GI values in the orthomosaic are in average 0.21 higher than the GI values from the ground spectral samples. In the case of the mission under clear sky, all the methods tend to underestimate the GI values of the orthomosaics. This is due to the way that different correction methods modify the bands differently, this was stated previously (Figure 23). The percentage RMSE for all the methods under overcast and clear sky conditions can be seen in Figure 25. The EC+ELC and the P+ELC correction methods have higher RMSE because they tend to have higher Red band values in relation to the Green band (Figure 23).

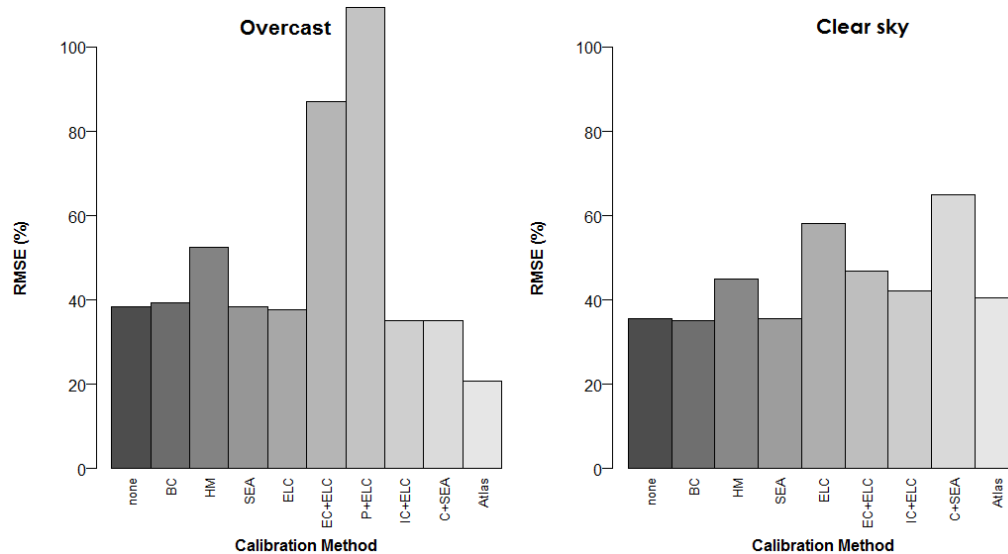


**Figure 25** RMSE statistics (%) for radiometric correction method comparison in the G/R index P+ELC stands for irradiance compensation with PAR and Empirical Line Calibration.

The use of the empirical line correction provided the same results as the GI values obtained from the orthomosaic without any radiometric correction. This is because the scaling factors of the G and R bands are similar when the missions are under overcast conditions. Under clear sky conditions, the brightness correction provided lower RMSE (35%). However, this method has more error when the sky is overcast because the transformation depends on the maximum brightness of the whole orthomosaic.

### 4.2.3. Structural indices

#### NDVI

NDVI values from the orthomosaics generated using the combination of irradiance compensation, empirical line calibration and sun elevation angle correction have lower RMSE in overcast and clear sky missions (Figure 26).

Comparing the calibration methods in the mission under overcast conditions (see Figure 26), C+SEA has the lowest RMSE (37%), followed by Atlas (38%), both methods tend to underestimate the NDVI values. In the case of the mission under clear sky, the NDVI values of all the orthomosaics present high RMSE. In the case of Atlas, the NDVI values are overestimated for pixels with bare soil and underestimated for pixels with vegetation. Atlas has values lower than 0.3 for crops. On the other hand, the irradiance compensation with empirical line calibration and SEA have underestimated NDVI values, with an RMSE of 83%.

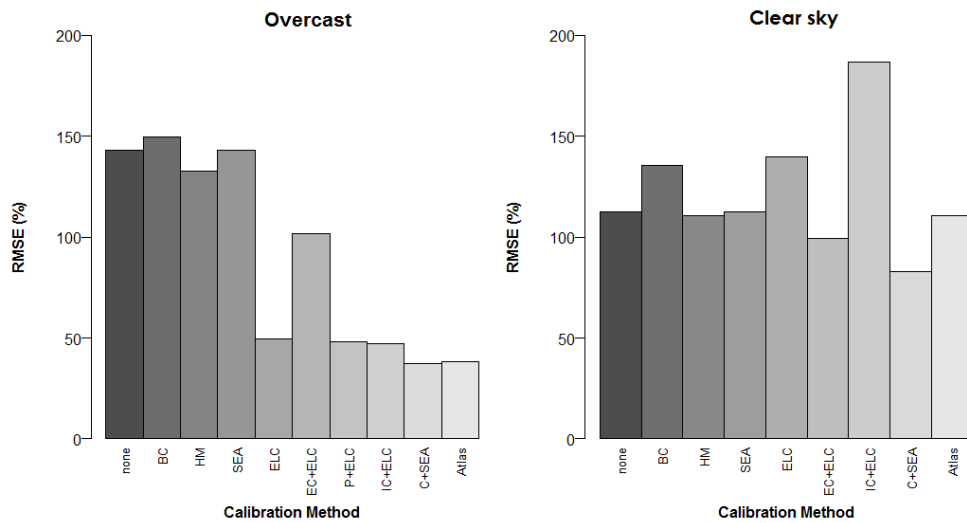


**Figure 26** RMSE statistics (%) for radiometric correction method comparison on the NDVI

### **NDRe**

NDRe values had lower RMSE in the orthomosaics generated using irradiance compensation with PAR data and empirical line calibration (Figure 27). Unfortunately, there was no P+ECL calibration for the clear sky mission, so it is not possible to determine if this method performs well under clear sky conditions. The NDRE values of the orthomosaic of EC+ELC from the clear sky mission have a RMSE of 83%. On the other hand, Atlas, BC, HM and SEA NDRe orthomosaic values are underestimated, having negative values and high RMSE. This is because these methods tend to have higher values in the Red edge band in relation to the other bands. This was stated in Figure 23, and their effects can be seen in figure 28.

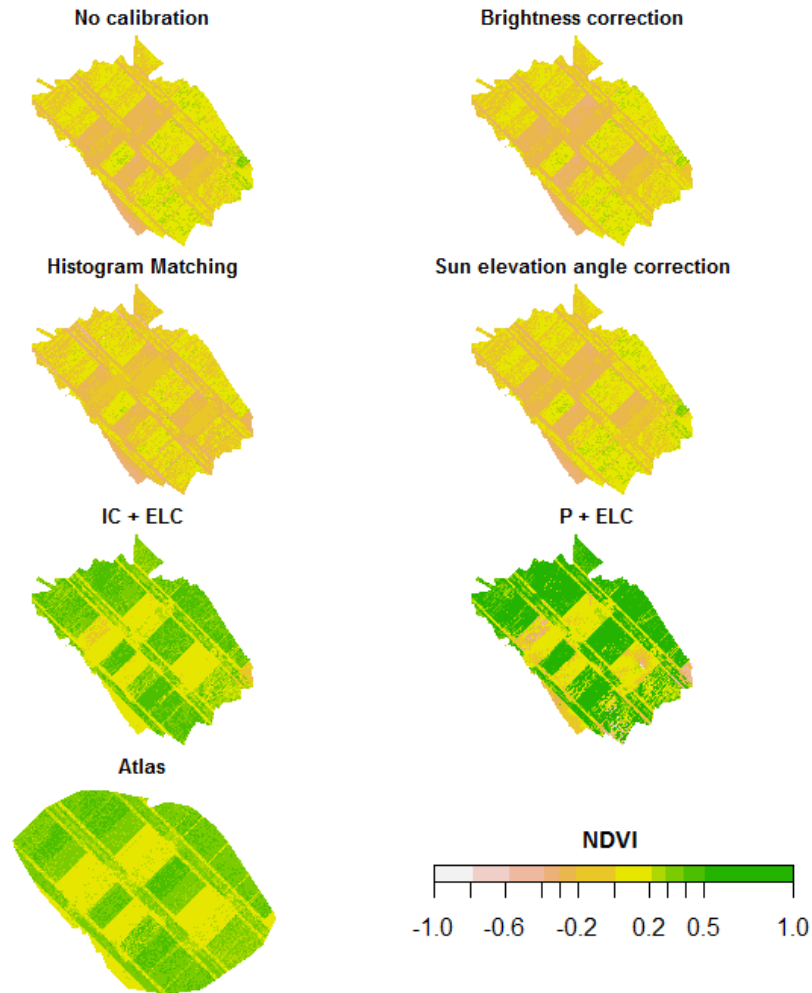


**Figure 27** NDVI of the orthomosaics generated with different radiometric correction methods for a mission under overcast conditions (Lönnpstorp 08-04-2017).

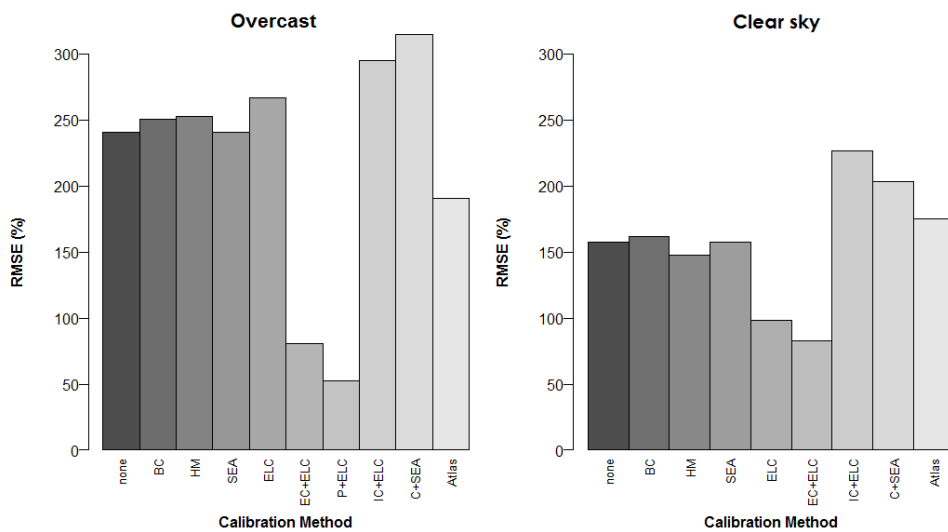


**Figure 28** RMSE statistics (%) for radiometric correction method comparison on the NDRi index

## EVI

The bands that are used to derive EVI are NIR, R and Blue band. In the GI comparison, it was possible to see that there were some errors in the correction of the Red band. In NDVI comparison it was possible to see that there are some errors in the correction of the NIR and Red band. The correction errors of the NIR band were more pronounced when the sky was clear. Since the EVI uses in addition the blue band, the combination of more bands leads to more error due to the error propagation.

The combination of irradiance compensation using PAR data and empirical line correction had the lowest RMSE in missions under overcast conditions, with RMSE values around 100%. Values of EVI were underestimated in both sky conditions because most of the methods tends to assign higher or the same values to the blue band in comparison to the Red band. Only P+ELC and Atlas tend to have lower values in Blue band (see Figure 23).

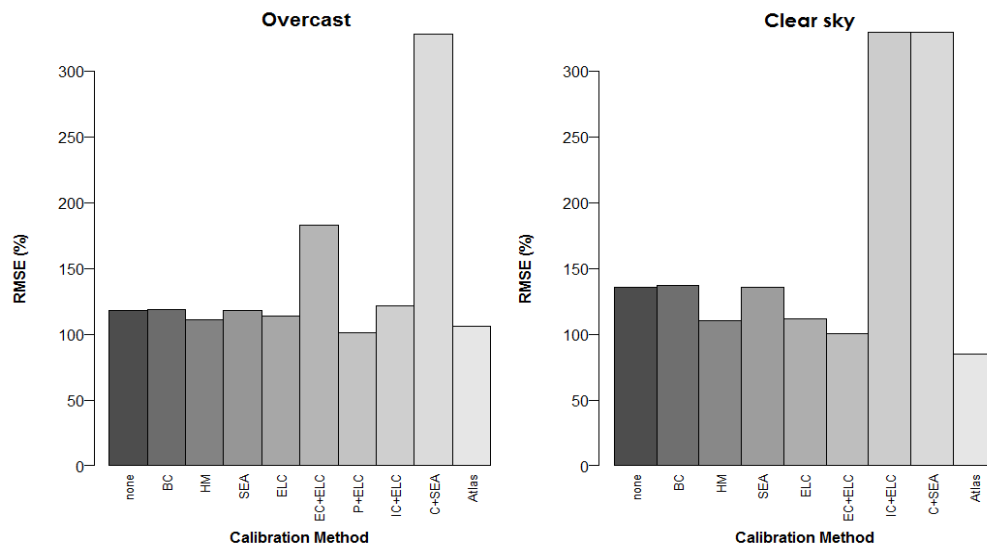
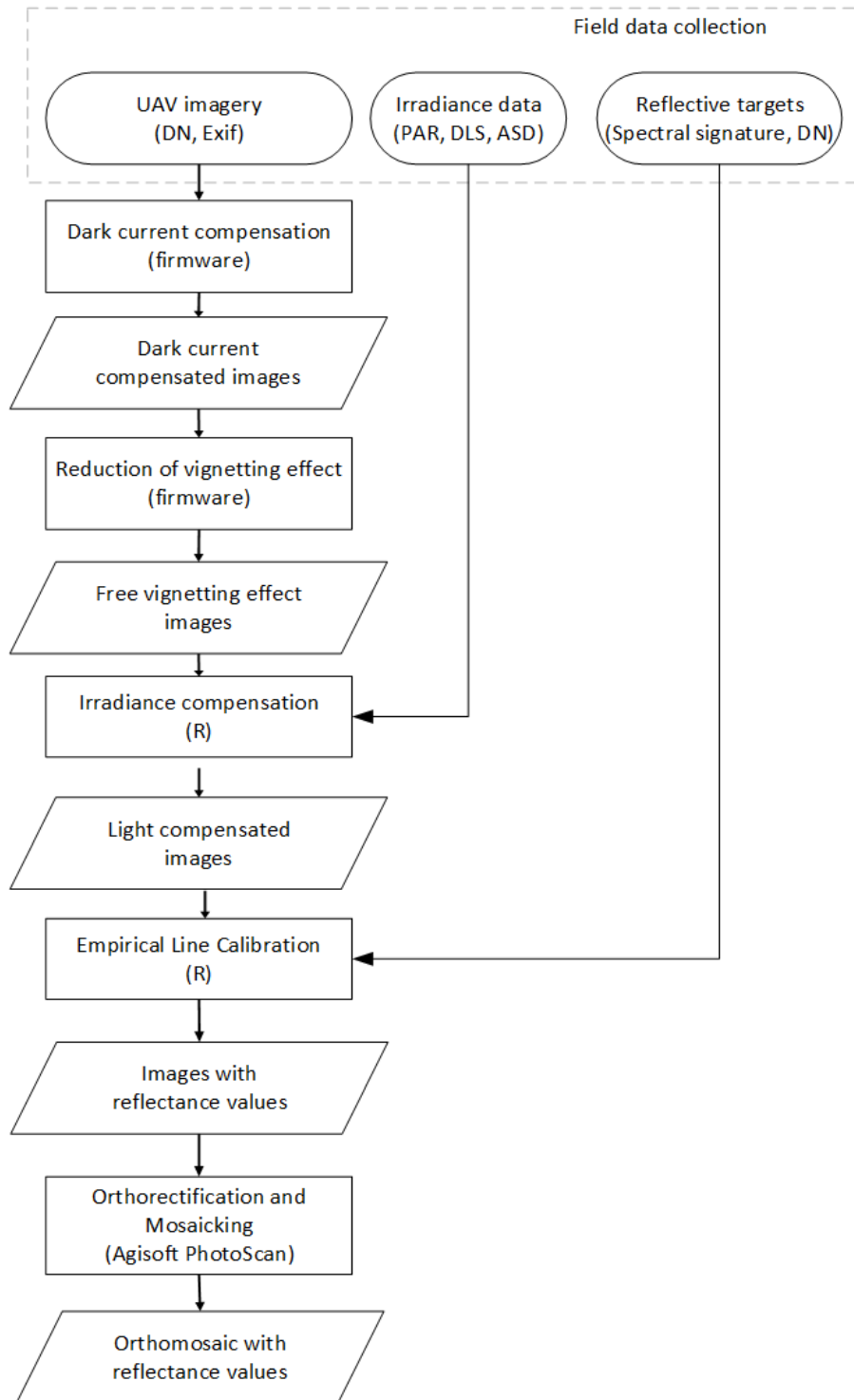


Figure 29 RMSE statistics (%) for radiometric correction method comparison on the EVI

### 4.3. Suggested radiometric correction workflow

As a result of the comparison of the different radiometric correction methods tested, the workflow in Figure 30 was developed as a suggestion for the radiometric correction of the Micasense Rededge camera. This workflow consists in two automatic steps performed by the camera firmware: (1) Dark current compensation and (2) Reduction of vignetting effect and two semi-automatic steps: (1) Irradiance compensation and (2) Empirical Line correction before generating a orthomosaic. All the processes are performed for each spectral band, having different irradiance and ELC correction factors per band per

mission. An R-script was developed to copy the exif data from original images to the calibrated ones to make them able to process them directly in Agisoft Photoscan. Scripts available on <https://github.com/xime377/RedEdge-calibration.git>.



**Figure 30** Suggested radiometric correction workflow.

It is important to mention that this workflow would provide less errors than working with uncalibrated data when vegetation indices are required. However, further research is needed to improve the accuracy of the correction.

## 5. Discussion

### 5.1. Incident light variation in UAV imagery

The results show that incident light variations affect the images significantly. Sun elevation angle and sky conditions (presence of clouds) are the principal causes of the light incident variation. The difference in the type of radiation affects the homogeneity of the UAV imagery and the radiometric correction, making the correction of UAV imagery more difficult from days with clear sky, when the direct radiation is predominant.

The reflective targets showed a stronger BRDF effect when the sky was clear. In addition, the BRDF was higher when their reflectance is higher, having stronger bidirectional effects for the targets with 44, 55 and 66% of reflectance. They were assessed with spectral measurements from different angles, but the variation was also observed in the pixel values comparison. When the sun elevation was higher, the DN values were higher (brighter) as well.

It is important to mention that the different angles assessed with the field spectrometer are referential, since the spectrometer was held by hand and not with a special equipment to fix a determined angle. The measurements from different angles were intended to cover the variation of reflectance captured from the camera in the UAV, simulating the movements of the sensor.

Analysis of the different sun elevation angles per band showed that the orthomosaics from missions with sun elevation angles from 29° to 44° are more homogeneous and have less shadows, since pixels with low DN values are less frequent. The lack of more missions on the same day with different sun elevation angle do not allow to get further conclusions.

This study shows that in order to obtain results that are radiometrically more accurate with less of the BRDF effect, the flights should be performed under overcast conditions. This differs from what many researchers suggest to fly over a clear sky (Lebourgeois et al. 2008; Rahman et al. 2014; Aasen et al. 2015).

The recommended survey time is similar to the one recommended by different authors: around two hours before or after the solar noon, when the sun elevation angle is between 20° and 40° in higher latitudes (Clemens 2012; Markelin 2013; Aasen et al. 2015).

## **5.2. Radiometric variations in vegetation indices**

Seven radiometric correction methods were tested, with nine methods in total when the empirical line calibration with irradiance compensation, and the sun elevation compensation were combined. In general terms, histogram matching and brightness correction are useful options for visualization purposes, but not to obtain accurate vegetation indices.

In missions without calibration targets or irradiance information, Lebourgeois et al. (2008) recommended using the solar elevation angle correction. This method could be useful because most of researchers recommend and perform the flights under clear sky and at around solar noon, therefore they are captured under similar atmospheric conditions. However, in this study, the results using only sun elevation angle correction provided RMSEs higher, or similar as working with raw DN values. It only improved the accuracy of the G/R ratio index, and only under clear sky conditions.

Regarding Atlas cloud software, the accuracy in the NDVI values of missions under overcast conditions are slightly better than the IC+ELC method, but lower compared with the IC+ELC+SEA. In this case, it is possible to note that, even if Atlas provided more accurate results in the calculation of GI and EVI, the drawback of this software is that it is a black-box where the information of how the data is processed is not available. This is something that researchers try to avoid. However, if data accuracy is not that important, Atlas is convenient since the only requirement is to upload the data in the cloud and wait 24 hours to get an orthomosaic, DSM and different vegetation indices.

The comparison of vegetation indices showed that using uncalibrated data may not provide the complete spectral depth required for vegetation analysis. This results coincide with research made by Lebourgeois et al. (2008) and Clemens (2012). The recommended workflow includes performing irradiance compensation and empirical line calibration. However, even if these methods gave lower RMSE value in the calculation of the majority of the VI compared, the values are too high to be considered accurate.

For this reason, the correction methods tested showed that the vegetation indices that capture small variations in vegetation like the chlorophyll index TCARI/OSAVI (Zarco-Tejada et al. 2013) are more prone to having higher errors. In addition, the combination of more bands with correction errors leads to higher errors, with EVI results being one example.

### **5.3. Limitations and advantages**

Regarding error propagation, Hakala et al. (2013) mentioned that in the combination of the irradiance compensation and ELC, inaccurate irradiance measurements or invalid assumptions reduce the accuracy of the overall correction. In this study, the combination of these methods provided in general lower RMSE. However, it is necessary to improve the irradiance compensation and the ELC to obtain more accurate results.

One source of error in the irradiance compensation is that the irradiance values from the DLS sensor and the field spectrometer differ. It was noticed that the values obtained from the DLS were lower than the values obtained with the spectrometer by 22% to 44%. This can be caused by the location of the DLS, which does not have a complete hemispherical view, since it is shadowed by the case of the Explorian. In addition, values corresponding to Red edge band are less accurate, this may be because this band is narrower and the DLS does not have cosine corrector, it has a light diffuser (Micasense, 2016). Hakala et al. (2013) recommended to use irradiance data from the field spectrometer with a cosine corrector if it is located in an open area without disturbance on the hemispherical view. Unfortunately, this was not possible to perform in this study because the field spectrometer only provided sporadic measurements instead of continuous data.

Irradiance compensation performed with PAR data provided better correction results for the NIR and Red edge band, providing better NDVI, NDR<sub>e</sub> and EVI results; however this sensor had one limitation: the PAR data consisted in only one value for 400 to 700 nm, where it was assumed that the irradiance in all the bands had the same behavior. Looking at figure 15 it is easy to realize, that even when there are overcast conditions, the irradiance values tend to be higher in the blue spectra (475 nm the central wavelength of the MS camera) and lower for the NIR (840 nm in the MS camera). These can be the causes of having

higher RMSE compared with the irradiance compensation performed with the DLS when working with Blue and Green bands.

The advantage of the PAR data is that, unlike the DLS, this data had a complete hemispherical view. Considering the irradiance distribution in the spectrum, sensors that provide incoming radiation values in at least the Green, Red and NIR bands, which are commonly used for vegetation mapping (Salami et al. 2014), could improve the irradiance compensation without using expensive equipment as a spectrometer. Empirical line calibration can be demanding in terms of field work and analysis, but it can provide results with lower errors using small amount of resources. There could be sophisticated radiometric correction methods, but they would be more demanding in terms of time and money. The present study tried to establish a feasible way to calibrate UAV images using open software and basic data available.

In the case of the ELC, once the offset per band is determined, only the gain needs to be estimated per band per mission. The fact that the linear regression was explained only in 98% indicates that there is some error due to the ignorance of the real correction equation. To obtain accurate results during the correction, it is important that the reflective targets have near-Lambertian properties. Unfortunately, Micasense and Mosaic Mill targets have strong bidirectional effects.

The Mosaic Mill targets are a relative cheap option of big reflective panels. However, their Lambertian properties decrease when the reflectance increases (the 10% target had less reflectance variation than the 44%). In addition, since they are made of felt, they tend to accumulate dust and the reflectance values could change over time, especially the brighter ones. For this reason, it is important to check from time to time the reflectance of the targets.

In order to obtain more accurate results, Micasense recommends to use Spectralon targets for research. Nevertheless, the price of a big enough Spectralon target is a limitation. A novel option, but not tested in this study, could be to use a target with near 0% of reflectance for the correction. The new pigment is called Vantablack (Nanosystems, UK) and targets of 10x10 cm (small size for UAV surveys) are available for educational purposes.

Assman et al. (2017) suggested to use targets with a reflectance value of 70% for vegetation mapping surveys. In order to survey snow covered surfaces a pure white standard higher than 90% reflectance

might be required. In this study, the high reflectance targets provided more BRDF effects and they were only used to generate the offset of the band equation. The reflectance target of 10% was the one used to obtain the gain per band equation. This could be the cause of having underestimated values, especially in the mission when the sky was clear.

Even though this study tested some absolute radiometric correction methods such as the irradiance compensation and empirical line calibration, these methods have instrument errors. It was mentioned previously that the DLS do not provide data as accurate as the field spectrometer. However, the spectrometer also has some limitations when taking spectral measurements. Since the reference panel (Spectralon) is used to transform all image cubes to reflectance, errors will propagate into every measurement if the panel does not have the 100% reflectance (i.e. when dirty or scratched). Unfortunately, this error cannot be quantified afterwards (Asd 1999).

#### **5.4. Recommendations**

For further studies, it is recommended to work with suitable reflectance targets. Targets size is important for the ELC. They need to be large enough to be seen in the image. Micasense targets are small and they cannot be distinguished when flying at higher altitudes. Mosaic Mill targets are bigger and they allowed the extraction of several pixels when performing the correction. Wang et al. (2015) and Assman et al. (2017) recommend to have a target with a minimum of 5 x 5 of the Ground Sampling Distance (GSD) (25 pixels), but 10 x 10 GSD (100 pixels) is desirable.

In order to avoid backscattering and saturation of the images, the location of the targets in relation to the sun angle and back scattering effects it is essential. For this reason, the mission and the targets should be designed in a way that the sun is at the back, avoiding the hot spot effect (Micasense 2015).

This study only considered dark current compensation, vignetting effect reduction and part of reflectance correction. The BRDF effects are not reduced with a simple empirical line correction, they need to be treated in different ways according to the surface type (Markelin 2013; Honkavaara 2014). Further studies to reduce the BRDF effect on this type of sensor are required.

Atmospheric correction was not considered in this study. The study areas and the low flying heights made possible to work with the assumption that atmospheric effects were minimum. However, in other areas

haze correction should be considered, especially in forested areas due to the presence of volatile organic compounds, or in polluted areas due to the presence of aerosols (Zarco-Tejada et al. 2013; Huang et al. 2016).

Another radiometric issue to consider in further research is the improvement of the sharpness in the images generated under overcast conditions. This could reduce the blur present in the Micasense Rededge images.

## 6. Conclusions

The main aim of this research was to develop a workflow to perform a radiometric correction of multispectral UAV imagery for vegetation mapping. In order to generate the workflow, the effect in incident light variations in UAV imagery was studied. Sun elevation angle and presence of clouds are the factors that influence the light variation in UAV images. The study of the sun elevation angle allowed to determine suitable hours for UAV surveys, at higher latitudes surveys in a range of 2 hours near solar noon provide less shadows because the sun elevation angle is between 20° and 40°.

The difference in the type of radiation affects the homogeneity of the UAV imagery and the radiometric correction, having more correction errors in UAV imagery from days with clear sky, when the direct radiation is predominant. The BRDF effects are less pronounced under overcast conditions, when the predominant incident radiation is diffuse.

The comparison of the radiometric corrections methods tested in different vegetation indices showed that the irradiance correction prior to an empirical line correction provide less errors than other methods. However the errors are still high when compared with ground spectral samples.

A simple workflow was developed for vegetation mapping purposes for the Micasense Rededge camera. It is suggested to use the automatic dark current corrected and automatic reduced vignetting effect images, plus an irradiance compensation and the use of empirical line correction to obtain reflectance values in single images before generating the orthomosaic. The radiometric correction process should be done by spectral band, having a new correction equation per mission due to the change on sky conditions.

Unfortunately this workflow will not provide accurate results in the calculation of vegetation indices that assess small variations like the case of chlorophyll indices or vegetation indices that combine several bands. Further research is needed to improve the accuracy of the correction.

Despite the need of improvements in radiometric correction methods of UAV imagery, the use of unmanned aerial vehicles equipped with a small multispectral sensor is a promising alternative for vegetation mapping.

## 7. References

- Aasen, H., A. Burkart, A. Bolten, and G. Bareth. 2015. Generating 3D hyperspectral information with lightweight UAV snapshot cameras for vegetation monitoring: From camera calibration to quality assurance. *ISPRS Journal of Photogrammetry and Remote Sensing* 108. International Society for Photogrammetry and Remote Sensing, Inc. (ISPRS): 245–259. doi:10.1016/j.isprsjprs.2015.08.002.
- Agisoft LLC. 2016. Agisoft PhotoScan User Manual: 37.
- Arnold, T., M. De Biasio, A. Fritz, and R. Leitner. 2013. UAV-based measurement of vegetation indices for environmental monitoring. In *2013 Seventh International Conference on Sensing Technology (ICST)*, 704–707. IEEE. doi:10.1109/ICSensT.2013.6727744.
- Asd. 1999. Analytical Spectral Devices , Inc . ( ASD ) Technical Guide: 144.
- Assman Jacob, and Kerby Jeff. 2017. High Latitude Drone Ecology Network – Multispectral Flight Protocol and Guidance Document – Drone Ecology Network.
- Clemens, S. 2012. Procedures for Correcting Digital Camera Imagery Acquired by the AggieAir Remote Sensing Platform 2012: 58.
- Dall ’asta, E., and R. R. Dicatea. 2014. A comparison of semiglobal and local dense matching algorithms for surface reconstruction. *The International Archives of the Photogrammetry, Remote Sensing and Spatial Information Sciences* XL-5. doi:10.5194/isprsarchives-XL-5-187-2014.
- Dunford, R., K. Michel, M. Gagnage, H. Piégay, and M.-L. Trémelo. 2009. Potential and constraints of Unmanned Aerial Vehicle technology for the characterization of Mediterranean riparian forest. *International Journal of Remote Sensing* 30. Taylor & Francis: 4915–4935. doi:10.1080/01431160903023025.
- Dunnington, D., and P. Harvey. 2016. Package “exifr” EXIF Image Data in R.
- Feng, Q., J. Liu, and J. Gong. 2015. UAV Remote Sensing for Urban Vegetation Mapping Using Random Forest and Texture Analysis. *Remote Sensing* 7. Multidisciplinary Digital Publishing Institute: 1074–1094. doi:10.3390/rs70101074.
- Fuyi, T., B. Boon Chun, M. Z. Mat Jafri, L. Hwee San, K. Abdullah, and N. Mohammad Tahrin. 2012. Land cover/use mapping using multi-band imageries captured by Cropcam Unmanned Aerial Vehicle Autopilot (UAV) over Penang Island, Malaysia. In *Proceedings of SPIE*, ed. E. M. Carapezza and H. J. White, 8540:85400S. SPIE. doi:10.1117/12.974911.
- Hajiyev, C., H. Ersin Soken, and S. Yenel Vural. 2015. *State Estimation and Control for Low-cost Unmanned Aerial Vehicles*. Cham: Springer International Publishing.
- Hakala, T., E. Honkavaara, H. Saari, J. Mäkynen, J. Kaivosoja, L. Pesonen, and I. Pölonen. 2013. Spectral Imaging From UAVs under varying illumination conditions. *ISPRS - International Archives of the Photogrammetry, Remote Sensing and Spatial Information Sciences* XL-1/W2: 189–194. doi:10.5194/isprsarchives-XL-1-W2-189-2013.
- Hollander, M., and D. A. Wolfe. 1973. *Nonparametric statistical methods*. Wiley.
- Honkavaara, E. 2014. State-of-the-art within radiometric correction of large-format aerial photogrammetric images Finnish Geodetic Institute ( FGI ).
- Huang, Y., W. Ding, and H. Li. 2016. Haze removal for UAV reconnaissance images using layered scattering model. *Chinese Journal of Aeronautics* 29: 502–511.

- doi:10.1016/j.cja.2016.01.012.
- Huang, Y. B., S. J. Thomson, W. C. Hoffmann, Y. Bin Lan, and B. K. Fritz. 2013. Development and prospect of unmanned aerial vehicle technologies for agricultural production management. *International Journal of Agricultural and Biological Engineering* 6: 1–10. doi:10.3965/j.ijabe.20130603.001.
- Humboldt State. 2015. Radiometric Corrections. *GSP 216 Introduction to Remote Sensing*.
- Japan Association of Remote Sensing. 1996. 9.1 Radiometric Correction.
- Jones, H., and R. Vaughan. 2010. *Remote Sensing of Vegetation: Principles, Techniques, and Applications*. Oxford and New York: Oxford University Press.
- Kuusik, A., and M. Paas. 2007. Radiometric correction of hemispherical images. *ISPRS Journal of Photogrammetry and Remote Sensing* 61: 405–413. doi:10.1016/j.isprsjprs.2006.10.005.
- Laliberte, A. 2009. Unmanned aerial vehicle-based remote sensing for rangeland assessment, monitoring, and management. *Journal of Applied Remote Sensing* 3: 33542. doi:10.1117/1.3216822.
- Lebourgeois, V., A. Bégué, S. Labbé, B. Mallavan, L. Prévot, and B. Roux. 2008. Can Commercial Digital Cameras Be Used as Multispectral Sensors? A Crop Monitoring Test. *Sensors* 8. Molecular Diversity Preservation International: 7300–7322. doi:10.3390/s8117300.
- Lillesand, T. M. ., and R. W. Kiefer. 2014. *Remote Sensing and Image Interpretation*. 7th ed. United States of America: John Wiley & Sons.
- Liu, Z., Y. Zhang, X. Yu, and C. Yuan. 2016. Unmanned surface vehicles: An overview of developments and challenges. *Annual Reviews in Control* 41. Elsevier Ltd: 71–93. doi:10.1016/j.arcontrol.2016.04.018.
- Majasalmi, T., M. Rautiainen, and P. Stenberg. 2014. Agricultural and Forest Meteorology Modeled and measured fPAR in a boreal forest : Validation and application of a new model. *Agricultural and Forest Meteorology* 189–190: 118–124. doi:10.1016/j.agrformet.2014.01.015.
- Markelin, L. 2013. Radiometric calibration, validation and correction of multispectral photogrammetric imagery. Aalto University School of Engineering.
- Matese, A., P. Toscano, S. Di Gennaro, L. Genesio, F. Vaccari, J. Primicerio, C. Belli, A. Zaldei, et al. 2015. Intercomparison of UAV, Aircraft and Satellite Remote Sensing Platforms for Precision Viticulture. *Remote Sensing* 7. Multidisciplinary Digital Publishing Institute: 2971–2990. doi:10.3390/rs70302971.
- Meshgi, K., and S. Ishii. 2015. Expanding histogram of colors with gridding to improve tracking accuracy. *Proceedings of the 14th IAPR International Conference on Machine Vision Applications, MVA 2015*: 475–479. doi:10.1109/MVA.2015.7153234.
- Micasense. 2015. MicaSense RedEdge TM 3 Multispectral Camera User Manual: 1–27.
- Micasense. 2016. Downwelling Light Sensor. Integration Guide and User Manual.
- Micasense. 2017. Atlas Cloud.
- Mitchell, H. B. 2010. Radiometric Calibration. In *Image Fusion*, 63–73. Berlin, Heidelberg: Springer Berlin Heidelberg. doi:10.1007/978-3-642-11216-4\_6.
- Nex, F., and F. Remondino. 2013. UAV for 3D mapping applications: a review. *Applied Geomatics* 6: 1–15. doi:10.1007/s12518-013-0120-x.
- Pedrotti, F. 2012. *Plant and Vegetation Mapping*. Berlin, Heidelberg: Springer Berlin Heidelberg.
- Pitchup AB. 2015. EXPLORIAN 4 Industrial UAV.

- Pix4D. 2017. Camera Requirements for Precision Agriculture – Support. *Support Pix4D*.
- Prosa, A., I. Colominaa, J. A. Navarroa, R. Antequerab, and P. Andrialb. 2013. Radiometric Block Adjustment and Digital Radiometric Model Generation. *ISPRS-International Archives of the Photogrammetry, Remote Sensing and Spatial Information Sciences* 1: 293–298.
- Rahman, M. M., J. N. Stanley, D. W. Lamb, and M. G. Trotter. 2014. Methodology for measuring fAPAR in crops using a combination of active optical and linear irradiance sensors: a case study in Triticale (X Triticosecale Wittmack). *Precision Agriculture* 15: 532–542. doi:10.1007/s11119-014-9349-6.
- Royston, J. P. 1982. Algorithm AS 181: The W Test for Normality. *Applied Statistics* 31: 176–180.
- Salamí, E., C. Barrado, and E. Pastor. 2014. UAV Flight Experiments Applied to the Remote Sensing of Vegetated Areas. *Remote Sensing* 6. Multidisciplinary Digital Publishing Institute: 11051–11081. doi:10.3390/rs61111051.
- Semyonov, D. 2011. Algorithms used in Photoscan.
- Sharma, R. C., K. Kajiwara, and Y. Honda. 2012. Automated extraction of canopy shadow fraction using unmanned helicopter-based color vegetation indices. *Trees* 27: 675–684. doi:10.1007/s00468-012-0822-4.
- Silleos, N. G., T. K. Alexandridis, I. Z. Gitas, and K. Perakis. 2006. Vegetation Indices: Advances Made in Biomass Estimation and Vegetation Monitoring in the Last 30 Years. *Geocarto International* 21: 21–28. doi:10.1080/10106040608542399.
- Stark, B., T. Zhao, and Y. Chen. 2016. An analysis of the effect of the bidirectional reflectance distribution function on remote sensing imagery accuracy from Small Unmanned Aircraft Systems. In *2016 International Conference on Unmanned Aircraft Systems (ICUAS)*, 1342–1350. IEEE. doi:10.1109/ICUAS.2016.7502566.
- The IDB Project. 2017. Index DataBase.
- The Weather Company LLC. 2017. Lund, Sweden Monthly Weather Forecast.
- US Department of Commerce, NOAA, E. S. R. L. 2017. NOAA Sunrise/Sunset and Solar Position Calculator.
- USGS National UAS Project Office. 2016. Unmanned Aircraft Systems Data Post-Processing. *Federal Aviation Administration*.
- Wang, C., and S. W. Myint. 2015. A Simplified Empirical Line Method of Radiometric Calibration for Small Unmanned Aircraft Systems-Based Remote Sensing. *IEEE Journal of Selected Topics in Applied Earth Observations and Remote Sensing* 8: 1876–1885. doi:10.1109/JSTARS.2015.2422716.
- Westoby, M. J., J. Brasington, N. F. Glasser, M. J. Hambrey, and J. M. Reynolds. 2012. “Structure-from-Motion” photogrammetry: A low-cost, effective tool for geoscience applications. *Geomorphology* 179. Elsevier B.V.: 300–314. doi:10.1016/j.geomorph.2012.08.021.
- Wijesingha, J. 2016. Geometric quality assessment of UAV-borne Remote Sensing ( RS ) products for Precision Agriculture ( PA ).
- Zarco-Tejada, P. J., A. Morales, L. Testi, and F. J. Villalobos. 2013. Spatio-temporal patterns of chlorophyll fluorescence and physiological and structural indices acquired from hyperspectral imagery as compared with carbon fluxes measured with eddy covariance. *Remote Sensing of Environment* 133. Elsevier Inc.: 102–115. doi:10.1016/j.rse.2013.02.003.
- Zweig, C. L., M. A. Burgess, H. F. Percival, and W. M. Kitchens. 2015. Use of Unmanned Aircraft

Systems to Delineate Fine-Scale Wetland Vegetation Communities. *Wetlands* 35: 303–309.  
doi:10.1007/s13157-014-0612-4.

## Department of Physical Geography and Ecosystem Science, Lund University

Lund University GEM thesis series are master theses written by students of the international master program on Geo-information Science and Earth Observation for Environmental Modelling and Management (GEM). The program is a cooperation of EU universities in Iceland, the Netherlands, Poland, Sweden and UK, as well a partner university in Australia. In this series only master thesis are included of students that performed their project at Lund University. Other theses of this program are available from the ITC, the Netherlands ([www.gem-msc.org](http://www.gem-msc.org) or [www.itc.nl](http://www.itc.nl)).

The student thesis reports are available at the Geo-Library, Department of Physical Geography and Ecosystem Science, University of Lund, Sölvegatan 12, S-223 62 Lund, Sweden. Report series started 2013. The complete list and electronic versions are also electronic available at the LUP student papers (<https://lup.lub.lu.se/student-papers/search/>) and through the Geo-library ([www.geobib.lu.se](http://www.geobib.lu.se)).

- 1 Soheila Younezadeh Jalili (2013) The effect of land use on land surface temperature in the Netherlands
- 2 Oskar Löfgren (2013) Using Worldview-2 satellite imagery to detect indicators of high species diversity in grasslands
- 3 Yang Zhou (2013) Inter-annual memory effects between Soil Moisture and NDVI in the Sahel
- 4 Efren Lopez Blanco (2014) Assessing the potential of embedding vegetation dynamics into a fire behaviour model: LPJ-GUESS-FARSITE
- 5 Anna Movsisyan (2014) Climate change impact on water and temperature conditions of forest soils: A case study related to the Swedish forestry sector
- 6 Liliana Carolina Castillo Villamor (2015) Technical assessment of GeoSUR and comparison with INSPIRE experience in the context of an environmental vulnerability analysis using GeoSUR data
- 7 Hossein Maazallahi (2015) Switching to the “Golden Age of Natural Gas” with a Focus on Shale Gas Exploitation: A Possible Bridge to Mitigate Climate Change?
- 8 Mohan Dev Joshi (2015) Impacts of Climate Change on *Abies spectabilis*: An approach integrating Maxent Model (MAXent) and Dynamic Vegetation Model (LPJ-GUESS)
- 9 Altaaf Mechiche-Alami (2015) Modelling future wheat yields in Spain with LPJ-GUESS and assessing the impacts of earlier planting dates
- 10 Koffi Unwana Saturday (2015) Petroleum activities, wetland utilization and livelihood changes in Southern Akwa Ibom State, Nigeria: 2003-2015
- 11 José Ignacio Díaz González (2016) Multi-objective optimisation algorithms for GIS-based multi-criteria decision analysis: an application for evacuation planning
- 12 Gunjan Sharma (2016) Land surface phenology as an indicator of performance of conservation policies like Natura2000

- 13 Chao Yang (2016) A Comparison of Four Methods of Diseases Mapping
- 14 Xinyi Dai (2016) Dam site selection using an integrated method of AHP and GIS for decision making support in Bortala, Northwest China
- 15 Jialong Duanmu (2016) A multi-scale based method for estimating coniferous forest aboveground biomass using low density airborne LiDAR data
- 16 Tanyaradzwa J. N. Muswera (2016) Modelling maize (*Zea Mays L.*) phenology using seasonal climate forecasts
- 17 Maria Angela Dissegna (2016) Improvement of the GPP estimations for Sudan using the evaporative fraction as water stress factor
- 18 Miguel G. Castro Gómez (2017) Joint use of Sentinel-1 and Sentinel-2 for land cover classification: A machine learning approach
- 19 Krishna Lamsal (2017) Identifying potential critical transitions in a forest ecosystem using satellite data
- 20 Maimoona Zehra Jawaid (2017) Glacial lake flood hazard assessment and modelling: a GIS perspective
- 21 Tracy Zaarour (2017) Application of GALDIT index in the Mediterranean region to assess vulnerability to sea water intrusion
- 22 Stephania Zabala (2017) Comparison of multi-temporal and multispectral Sentinel-2 and UAV (unmanned aerial vehicle) imagery for crop type mapping
- 23 Ximena Tagle (2017) Radiometric calibration of unmanned aerial vehicle remote sensing imagery for vegetation mapping